



Article

Multi-Channel Spectral Band Adjustment Factors for Thermal Infrared Measurements of Geostationary Passive Imagers

Dennis Piontek ^{1,*} , Luca Bugliaro ¹ , Richard Müller ² , Lukas Muser ^{3,†} and Matthias Jerg ²

¹ Deutsches Zentrum für Luft- und Raumfahrt (DLR), Institut für Physik der Atmosphäre, 82234 Oberpfaffenhofen, Germany

² Deutscher Wetterdienst (DWD), 63067 Offenbach, Germany

³ Karlsruhe Institute of Technology (KIT), Institute of Meteorology and Climate Research, 76131 Karlsruhe, Germany

* Correspondence: dennis.piontek@dlr.de

† Current address: Alfred Wegener Institute for Polar and Marine Research (AWI), 27570 Bremerhaven, Germany.

Abstract: The newest and upcoming geostationary passive imagers have thermal infrared channels comparable to those of more established instruments, but their spectral response functions still differ significantly. Therefore, retrievals developed for a certain type of radiometer cannot simply be applied to another imager. Here, a set of spectral band adjustment factors is determined for MSG/SEVIRI, Himawari-8/AHI, and MTG1/FCI from a training dataset based on MetOp/IASI hyperspectral observations. These correction functions allow to turn the observation of one sensor into an analogue observation of another sensor. This way, the same satellite retrieval—that has been usually developed for a specific instrument with a specific spectral response function—can be applied to produce long time series that go beyond one single satellite/satellite series or to cover the entire geostationary ring in a consistent way. It is shown that the mean uncorrected brightness temperature differences between corresponding channels of two imagers can be >1 K, in particular for the channels centered around 13.4 μm in the carbon dioxide absorption band and even when comparing different imager realizations of the same series, such as the four SEVIRI sensors aboard MSG1 to MSG4. The spectral band adjustment factors can remove the bias and even reduce the standard deviation in the brightness temperature difference by more than 80%, with the effect being dependent on the spectral channel and the complexity of the correction function. Further tests include the application of the spectral band adjustment factors in combination with (a) a volcanic ash cloud retrieval to Himawari-8/AHI observations of the Raikoke eruption 2019 and a comparison to an ICON-ART model simulation, and (b) an ice cloud retrieval to simulated MTG1/FCI test data with the outcome compared to the retrieval results using real MSG3/SEVIRI measurements for the same scene.

Keywords: passive remote sensing; geostationary satellite imager; spectral band adjustment factor; Meteosat; Himawari



Citation: Piontek, D.; Bugliaro, L.; Müller, R.; Muser, L.; Jerg, M. Multi-Channel Spectral Band Adjustment Factors for Thermal Infrared Measurements of Geostationary Passive Imagers. *Remote Sens.* **2023**, *15*, 1247. <https://doi.org/10.3390/rs15051247>

Academic Editor: Carmine Serio

Received: 24 January 2023

Revised: 16 February 2023

Accepted: 20 February 2023

Published: 24 February 2023



Copyright: © 2023 by the authors. Licensee MDPI, Basel, Switzerland. This article is an open access article distributed under the terms and conditions of the Creative Commons Attribution (CC BY) license (<https://creativecommons.org/licenses/by/4.0/>).

1. Introduction

Numerous passive moderate- to high-resolution imagers are deployed in Earth's geostationary orbit, with their fields of regard covering nearly the full globe except for the polar regions (Figure 1). This includes the radiometers aboard the satellites of *Meteosat Second Generation* (MSG) [1], the *Geostationary Operational Environmental Satellite* (GOES) [2,3], Himawari [4], Feng-Yun [5], and the upcoming *Meteosat Third Generation* (MTG) [6]. Their measurements are processed with a multitude of retrieval algorithms to derive information on the atmosphere and the surface. The most basic detection methods for water clouds or volcanic ash simply rely on one or multiple threshold criteria with respect to the measured radiation [7,8]. More advanced retrievals utilize extensive precalculated look-up tables based on radiative transfer calculations [9,10] or are trained with real satellite observations [11,12]. Furthermore, deep learning methods (i.e., artificial neural networks)

are increasingly being used to derive physical parameters from satellite data [13,14]. In all these cases, specific imagers are used to retrieve information of the atmosphere or the surface.

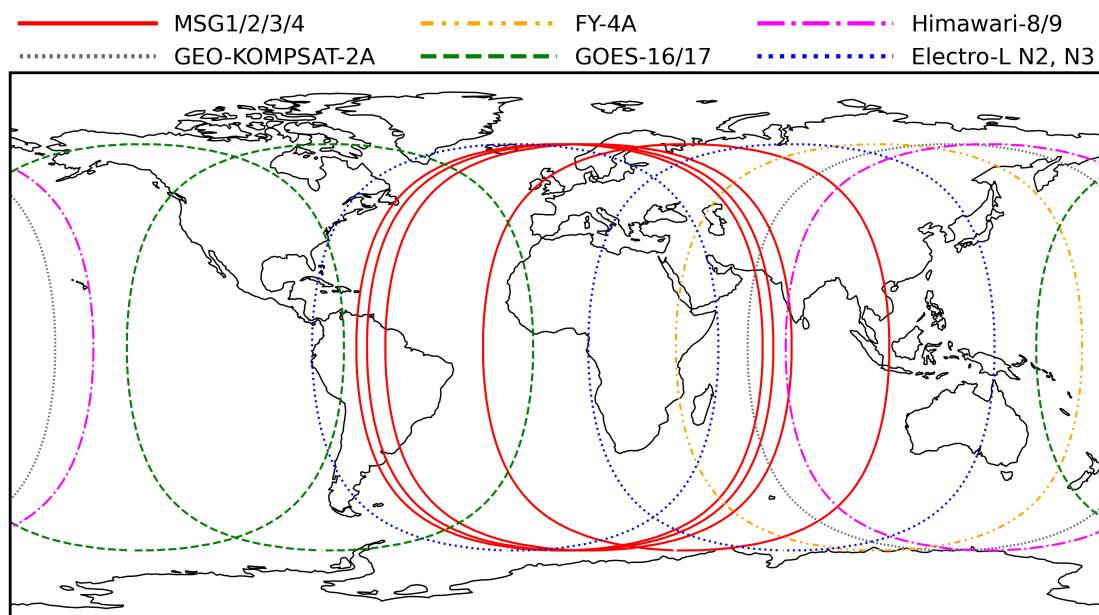


Figure 1. Field of view of all currently active advanced moderate-resolution optical imagers aboard geostationary satellites. The colored borders correspond to viewing zenith angles of 75°.

Unfortunately, orbital imagers differ in their temporal and spatial sampling rates, as well as in their spectral channels; even different instruments of the same series can have significant differences in the spectral channels (see Section 2.1 for details). As a consequence, methods developed for a specific instrument cannot easily be adapted to another instrument. This is especially true for artificial neural networks for which single internal parameters are not necessarily directly related to specific physical quantities as is usually the case for, e.g., threshold-based detection schemes.

There are two possible options to overcome this problem: firstly, the retrieval algorithms could be recreated with new training datasets/look-up tables, which might be time-consuming. In some cases, this might be even impossible as, for instance, some algorithms exploit multi-year collocated observations of passive, geostationary imagers and an active, polar-orbiting lidar [13,15,16]. For the newest imagers, sufficient amounts of such collocated measurements might not exist. This is particularly true for the MTG satellites of which the first unit was launched by end of 2022.

Secondly, the spectral channels of the new imager are corrected for the differences with respect to the older instrument for which the method was originally created. Such corrections are called *spectral band adjustment factors* (SBAFs). In simple terms, high-resolution spectra (e.g., from a radiative transfer simulation or from a third instrument) are convolved with the instrument-specific *spectral response functions* (SRFs) to derive synthetic imager measurements for two different imagers for a common spectrum. The two synthetic observations are then related by the SBAFs (see Section 2.4.1 for details). In this way, the original retrieval method can be used with data of the new imager. For example, Chander et al. [17] derived linear SBAFs for bands in the visual spectrum of the instruments *Enhanced Thematic Mapper Plus* (ETM+) on *Landsat 7* and the *Moderate Resolution Imaging Spectroradiometer* (MODIS) on the *Terra* satellite. For this purpose, the authors used three different datasets: (a) collocated nearly-simultaneous observations of a test site, (b) hyperspectra from the *Hyperion* instrument on *Earth Observing-1*, and (c) hyperspectra from the *Scanning Imaging Absorption Spectrometer for Atmospheric Cartography* (SCIAMACHY) aboard the *ENVironmental SATellite* (ENVISAT). Also Doelling et al. [18] calculated linear SBAFs between two

channels of different imagers using SCIAMACHY data. Building upon this approach, Scarino et al. [19] created an online tool to calculate SBAFs for visible and near-infrared channels. Considering the impact on the SBAFs, they found that the choice of the instrument providing the high-resolution spectra is much less significant than the selection of the hyperspectra with respect to atmospheric, viewing, and insolation conditions. The web tool was extended to cover spectral data from SCIAMACHY, Hyperion, the *Global Ozone Monitoring Experiment-2* (GOME-2), the *Infrared Atmospheric Sounding Interferometer* (IASI), and the *Atmospheric Infrared Sounder* (AIRS). It allows different subsetting specifications [20] and SBAFs up to third order (instead of only linear correction factors, [21]). Using the approach of SBAFs, also other ideas were realized, e.g., Qin and McVicar [22] used Hyperion spectra to derive analog measurements of the *Advanced Himawari Imager* (AHI) on Himawari-8 from MODIS and *Visible Infrared Imaging Radiometer Suite* (VIIRS) observations, thereby effectively creating a virtual dual-view sensor.

The concept of SBAFs is also related to the work on the inter-calibration of geostationary imagers. Gunshor et al. [23] used spatially and temporally collocated observations of AIRS and various geostationary imagers. The AIRS spectra were convolved with the SRFs of the imagers and the results were compared to the imagers measurements to determine their uncertainties and biases. In this case, AIRS was used as a standard reference, i.e., AIRS was assumed to be perfectly calibrated. Collocation included simultaneous geostationary nadir observations in an area of $\pm 10^\circ$ latitude/longitude with AIRS scan angles up to $\pm 10^\circ$ to minimize differences in the viewing geometry. Satellite data were smoothed on $100 \text{ km} \times 100 \text{ km}$ and maximal temporal separation was limited to 15 min. Hewison et al. [24] performed a similar study using IASI measurements as reference. Their collocation dataset included only nighttime measurements to avoid azimuthal anisotropies, which can be in the order of $\pm 3 \text{ K}$ [25]. Spatial collocation was limited to displacements of 6 km with averaging of all included pixels. Temporal collocation was confined to 5 min. Differences in the secant of the viewing zenith angles were < 0.01 to ensure similar viewing geometries, and outliers (i.e., radiance differences > 3 standard deviations) were excluded. Spectral corrections of this kind are provided by the *Global Space-based Inter-Calibration System* (GSICS). Related approaches were used in various other studies as well [26–29]. If geostationary imagers have a spatial overlap in their fields of view, it is also possible to directly inter-compare their measurements, e.g., Rublev et al. [30] presented a corresponding study for a Russian imager at 76°E and MSG3 at 0°E .

The situation is complicated by the fact that the SRFs might experience shifts for each channel during the satellite lifetime and wavelength-dependent degradation [31–33]. Quast et al. [32] demonstrated that the reduction of the SRF is stronger in the blue/ultraviolet than in the red/near-infrared regime at the example of the visible channel of the *Meteosat First Generation* imager and, thus, stated that the effect is more obvious for broadband imagers than for instruments with rather narrow channels.

This study pursues two goals. First, complex SBAFs including multiple input channels to derive an output channel (instead of the usual 1-to-1 relations) and functions of higher order (instead of only linear or at most third-order polynomials) are tested. The work concentrates on the thermal infrared regime and on mappings towards the *Spinning Enhanced Visible and InfraRed Imager* (SEVIRI) on MSG. Second, the combination of SBAFs with retrievals tailored for MSG2/SEVIRI is investigated, namely *Volcanic Ash Cloud properties Obtained from SEVIRI* (VACOS) [34] and *Cirrus Properties from SEVIRI* (CiPS) [15]. Section 2 introduces the imagers, retrievals, reference data, and the derivation of the SBAFs. The developed SBAFs are applied and tested in Section 3, individually by combining pairs of Meteosat satellites as well as in combination with VACOS and CiPS. Results are discussed in Section 4. Finally, conclusions and an outlook are given.

2. Materials and Methods

2.1. Satellite Data

2.1.1. MSG/SEVIRI

The main satellite instrument utilized in this work is the *Spinning Enhanced Visible and InfraRed Imager* (SEVIRI), which is the passive imager aboard the geostationary *Meteosat Second Generation* (MSG) satellites. SEVIRI has 12 channels. Three bands are in the visible and near-infrared spectrum and are centered at 0.6, 0.8, and 1.6 μm . Eight bands are in the thermal infrared at 3.9, 6.2, 7.3, 8.7, 9.7, 10.8, 12, and 13.4 μm . Finally, one channel is a high-resolution visible (HRV) broadband, covering roughly 0.4–1.1 μm and half of the SEVIRI disc at each revolution. The spectral sensitivity of the channels is characterized by the SRFs, which are shown in Figure 2 for the thermal bands of MSG2. Some of the channels cover specific components of the atmosphere, i.e., the channels at 6.2 and 7.3 μm are influenced by water vapor, whereas the bands at 9.7 and 13.4 μm are affected by ozone and carbon dioxide, respectively. Other channels, e.g., at 8.7, 10.8, and 12 μm are located within the atmospheric window and, thus, are used to observe meteorological clouds, aerosols or the Earth's surface [1]. Radiances in the visible channels are converted to reflectances, whereas brightness temperatures are derived for the measurements in the thermal channels. The latter corresponds to a temperature T such that the convolution of Planck's function $B(\lambda, T)$ at wavelength λ and the normalized SRF equals the measured radiance [35]. Typical measurement noise of the thermal channels is in the size range 0.04–0.24 K [36]. The spatial resolution at the sub-satellite point is 1 km for the HRV band and 3 km for the other channels; the temporal resolution for full disc coverage is 15 min [1].

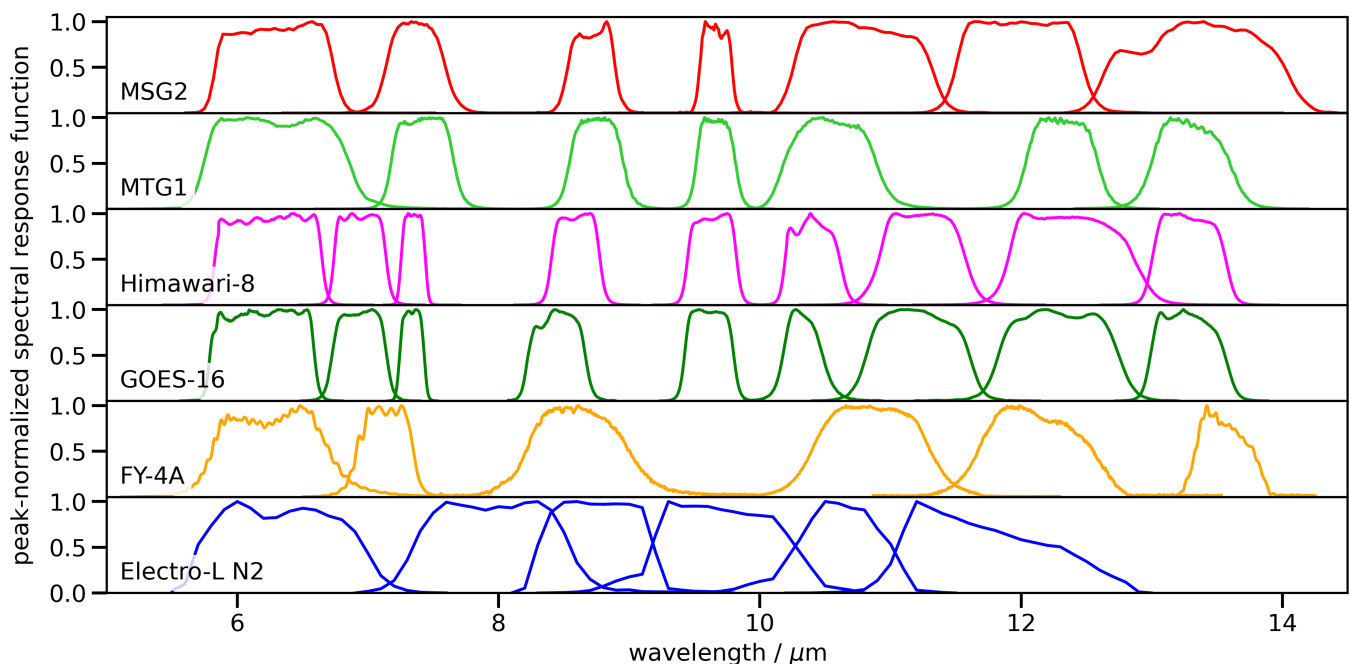


Figure 2. Peak-normalized spectral response functions of the currently active/planned, advanced imagers aboard geostationary satellites. Only channels between 5 and 15 μm are shown. Data from [37].

Starting in 2002, four MSG satellites (MSG1 to MSG4) have been launched, named *Meteosat-8* to 11. As of 3 January 2023, the current main operational satellite (MSG4) is located at 0°E. MSG3 operates at 9.5°E in rapid-scan mode, covering only the upper third of the SEVIRI disc (including Northern Africa and Europe) but at an increased temporal resolution of 5 min. MSG2 was moved to 45.5°E to cover the Indian Ocean (*Indian Ocean Data Coverage*, IODC). MSG1 provided IODC until summer 2022, when it was retired [38].

2.1.2. MTG/FCI

Starting from 2022, the new satellite series *Meteosat Third Generation* (MTG) is launched to successively replace MSG [39]. Those carry the *Flexible Combined Imager* (FCI), which has 16 channels. MTG/FCI has similar channels in the thermal infrared as MSG/SEVIRI, with central wavelengths slightly shifted and a smaller bandwidth (see Figure 2) to better isolate the spectral signature of the atmospheric components. MTG/FCI has a higher temporal and spatial resolution of 10 min and ≤ 2 km, respectively [6,40]. The first unit, MTG1, will be deployed at 0°E and, thus, replace MSG4.

Since there are no real MTG1/FCI observations yet, the *MTGTD-360 Spectrally Representative FCI L1C Test Products* are used [41]. This dataset consists of synthetic MTG1/FCI observations for a time period of 24 h on 20 September 2017, with the thermal infrared data simulated with RTTOV and adopting a plane parallel and independent pixel approximation. Input data were a combination of atmospheric model data from the *European Centre for Medium-Range Weather Forecasts* (ECMWF), aerosol information from the *Copernicus Atmosphere Monitoring System* (CAMS), and cloud products retrieved from MSG3/SEVIRI; real SRFs of MTG1/FCI were used.

2.1.3. Himawari/AHI

Since 2014, the Japanese Himawari satellites are in operation, carrying the *Advanced Himawari Imager* (AHI). AHI has 16 channels, thereof 10 in the thermal infrared. Compared to SEVIRI, there is an additional band in the water vapor regime at 6.9 μm , and in the atmospheric window, such that AHI has channels at 10.4, 11.2, and 12.4 μm (see Figure 2). Just as MTG/FCI, Himawari/AHI has a higher temporal and spatial resolution of 10 min and 2 km, respectively [4]. AHI has similar properties as the *Advanced Baseline Imager* (ABI) aboard the *Geostationary Operational Environmental Satellite* (GOES) since GOES-16 [2,3] and the *Advanced Meteorological Imager* (AMI) aboard GEO-KOMPSAT-2A [42] with respect to the spectral channels, their central wavelengths, bandwidths, and spatial resolution as they all belong to the same imager series [43]. The two units Himawari-8 (backup) and Himawari-9 (operational) are both located at 140.7°E. They switched roles by end of 2022 [44].

2.1.4. MetOp/IASI

The *Meteorological Operational satellites* (MetOp) are active since 2006. They are on a sun-synchronous polar orbit with an equator crossing time of 09:30 local time, and carry, among others, the *Infrared Atmospheric Sounding Interferometer* (IASI). IASI is a cross-track scanning Michelson interferometer with 120 measurements per scan, with a diameter of 12 km for the measurement at the sub-satellite point. It covers the spectral range 645–2760 cm^{-1} (3.62–15.5 μm) at a resolution of 0.25 cm^{-1} (thus, 8461 channels). IASI was found to be very stable and is regularly used in inter-calibration studies [45].

2.2. The ICON-ART Model

ICON is the *ICOsahedral Nonhydrostatic weather and climate model*. It solves the full three-dimensional compressible and non-hydrostatic Navier–Stokes equations [46]. Therefore, the model atmosphere is discretized on a horizontally unstructured triangular grid. To account for the emission, transport, physicochemical transformation, and removal of aerosols and reactive trace gases in ICON, the ART (*Aerosols and Reactive Trace gases*) module is used [47–50]. ICON-ART can seamlessly be applied from global to local scales [51,52]. In this work, results of a global simulation of the Raikoke 2019 eruption are presented.

2.3. Satellite Retrievals

2.3.1. VACOS

Volcanic Ash Cloud properties Obtained from SEVIRI (VACOS) allows the detection of volcanic ash clouds and the retrieval of the volcanic ash optical depth at 10.8 μm (volcanic ash produces a typical extinction signal at 8–12 μm [53–55]) which can be related to the

mass load, the effective particle radius, and the cloud top height from thermal infrared measurements of MSG/SEVIRI and auxiliary data, including time, geographical location, viewing zenith angle, land/sea mask, surface temperature, and total column water/water vapor/ozone estimates from the numerical weather prediction model of ECMWF. It consists of four artificial neural networks, which were trained with an extensive dataset of synthetic infrared observations of MSG2/SEVIRI. The training data were composed such that they cover a widest possible range of atmospheric states (using ECMWF ERA5 reanalysis data), geographic coordinates, and volcanic ash cloud types [34]. A variety of volcanic ash types with different compositions were considered [55]. VACOS was comprehensively validated using simulated test data, retrievals of air- and spaceborne lidars, and in situ data from aircraft campaigns, especially for the eruptions of Eyjafjallajökull (2010) and Puyehue-Cordón Caulle (2011) [56]. It was selected as reference for testing various volcanic ash transport and dispersion models [57,58].

2.3.2. CiPS

Cirrus Properties from SEVIRI (CiPS) allows the detection of cirrus clouds, the retrieval of the ice optical thickness at 532 nm, the ice water path, the ice cloud top height, and an opacity flag from thermal infrared measurements of MSG/SEVIRI and auxiliary data, including time, latitude, viewing zenith angle, land/sea mask, snow/ice flag, and surface temperature from ECMWF. It uses four artificial neural networks that were trained with a dataset of collocated passive MSG2/SEVIRI observations and active measurements from *Cloud Aerosol Lidar with Orthogonal Polarization* (CALIOP) aboard *Cloud-Aerosol Lidar and Infrared Pathfinder Satellite Observation* (CALIPSO), using the CALIPSO/CALIOP data as truth during the training [15]. CiPS was extensively validated [59] and applied in studies on natural cirrus and anthropogenic contrails [60–62].

2.4. Spectral Band Adjustment Factors

2.4.1. Definition

The analog radiation measurement of the satellite imager is converted into digital counts and then turned into an effective radiance L_{eff} via a relationship based on a preceding calibration [63,64]. This L_{eff} corresponds to the convolution of the upwelling top-of-atmosphere radiance $L_{\text{spectrum}}(\nu)$, depending on the wavenumber ν , and the spectral response function $\text{SRF}(\nu)$, describing the sensitivity of the spectral bands:

$$L_{\text{eff}} = \frac{\int_0^{\infty} L_{\text{spectrum}}(\nu) \times \text{SRF}(\nu) d\nu}{\int_0^{\infty} \text{SRF}(\nu) d\nu}. \quad (1)$$

As the SRF is instrument-dependent, each satellite measures slightly different values for L_{eff} , even if observing the same spectrum. For example, Figure 3 shows the SRFs of SEVIRI aboard MSG1–4 and AHI aboard Himawari-8/9. Considering the carbon dioxide channels of both imager series, they are centered roughly at the same wavelength but vary strongly in their width, leading to an impact on L_{eff} . Similarly, also the SRFs of the different SEVIRI imagers are not identical, although the differences are much smaller. For simplicity, the possible channel and wavelength-dependent degradation of the SRFs is neglected in this work.

To address and correct for the differences in L_{eff} , one applies *spectral band adjustment factors* (SBAFs). For instance, L_{eff} of analog channels of two imagers A and B at some central wavelength λ_m can be related by a function f such that

$$L_{\text{eff},A,\lambda_m} = f(L_{\text{eff},B,\lambda_m}) \quad (2)$$

with the coefficients of f being the SBAFs for these two channels (e.g., slope and offset if f is linear). Starting from the linear case, three different extensions are possible for f : First, by considering more complex functions such as polynomials of higher degree. This allows to handle nonlinearities between $L_{\text{eff},A,\lambda_m}$ and $L_{\text{eff},B,\lambda_m}$ (see Supplementary Material), possibly

caused by the temperature dependence of Planck's function (e.g., the peak is lower and decreases less steeply for lower temperatures, such that SRFs slightly shifted relatively to each other might still produce comparable measurements). Second, one can benefit from using multiple channels of imager B to derive a single channel of imager A, i.e.,

$$L_{\text{eff},A,\lambda_m} = f(L_{\text{eff},B,\lambda_1}, L_{\text{eff},B,\lambda_2}, \dots, L_{\text{eff},B,\lambda_N}). \quad (3)$$

This can be explained by the fact that sometimes a single channel of imager A has an overlap with multiple channels of imager B (see Figure 2), either due to the width or the shifted central wavelength of imager A's channel. Furthermore, also channels without spectral overlap might still correlate because, e.g., all thermal satellite measurements are affected to varying degrees by the Earth's surface temperature, and some channels correlate due to a common sensitivity to specific atmospheric constituents, e.g., the atmospheric window channels or the water vapor channels. Third, additional auxiliary quantities can be used as input to f . For example, there are obvious dependencies of the deviation of $L_{\text{eff},A,\lambda_m}$ and $L_{\text{eff},B,\lambda_m}$ on the latitude and a bit weaker on the solar zenith angle (possibly related to the previously mentioned temperature-dependent nonlinearities), whereas no related dependence on the longitude, the viewing zenith angle or the surface type can be observed (see Supplementary Material). Combining all three extensions leads to the approach

$$f(I_1, I_2, \dots, I_N) = \sum_{\substack{k_1, k_2, \dots, k_N \text{ with } k_i \geq 0 \\ 0 \leq \sum_{i=1}^N k_i \leq D}} c_{k_1, k_2, \dots, k_N} \cdot I_1^{k_1} \cdot I_2^{k_2} \cdot \dots \cdot I_N^{k_N} \quad (4)$$

with the inputs I_m being either one of the effective radiances of imager B (i.e., $L_{\text{eff},B,\lambda_m}$) or the latitude, N the number of inputs, and D the maximum total degree. For example, for $N = 2$ and $D = 2$ and using two effective radiances as input leads to

$$f(L_{\text{eff},B,\lambda_1}, L_{\text{eff},B,\lambda_2}) = c_0 + c_1 L_{\text{eff},B,\lambda_1} + c_2 L_{\text{eff},B,\lambda_2} + c_3 L_{\text{eff},B,\lambda_1} L_{\text{eff},B,\lambda_2} + c_4 L_{\text{eff},B,\lambda_1}^2 + c_5 L_{\text{eff},B,\lambda_2}^2. \quad (5)$$

The simplest assumption,

$$L_{\text{eff},A,\lambda_m} = L_{\text{eff},B,\lambda_m}, \quad (6)$$

is denoted *naive SBAFs* in the following and does not consider any spectral correction.

For the comparison of MSG/SEVIRI and Himawari/AHI, the corresponding channels are indicated by the arrows in Figure 3. For the 10.8 μm channel of MSG/SEVIRI, there are two possible corresponding channels at Himawari-8/AHI, such that both candidates can be used in this case; for the naive SBAFs, the mean of the two channels is related to the 10.8 μm band of MSG/SEVIRI.

2.4.2. Composition of the Training Dataset

A large dataset of corresponding effective radiances is needed to fit the SBAFs. Here, we use all-sky hyperspectra from MetOp/IASI to calculate them. Four days are chosen to cover the seasonal variability of the Earth's atmosphere (the 15th January, April, July, and October in 2010). For each day, all 14 orbits are used to achieve nearly global coverage. From the resulting 56 orbits, a subset of 51,690 samples was considered. Figure 4 shows their distribution with respect to geographical coordinates, viewing zenith angle and solar zenith angle. As can be seen, the samples cover relatively uniformly the full globe. Viewing zenith angles are limited by the MetOp/IASI observations to 60° . Solar zenith angles vary between roughly 30° and 150° (when the solar zenith angle is larger than 90° , the Sun is below the horizon). However, there is a relation between latitude and solar zenith angle given by the orbital trajectory of MetOp. For example, there are no equatorial samples with solar zenith angles between 60° and 90° .

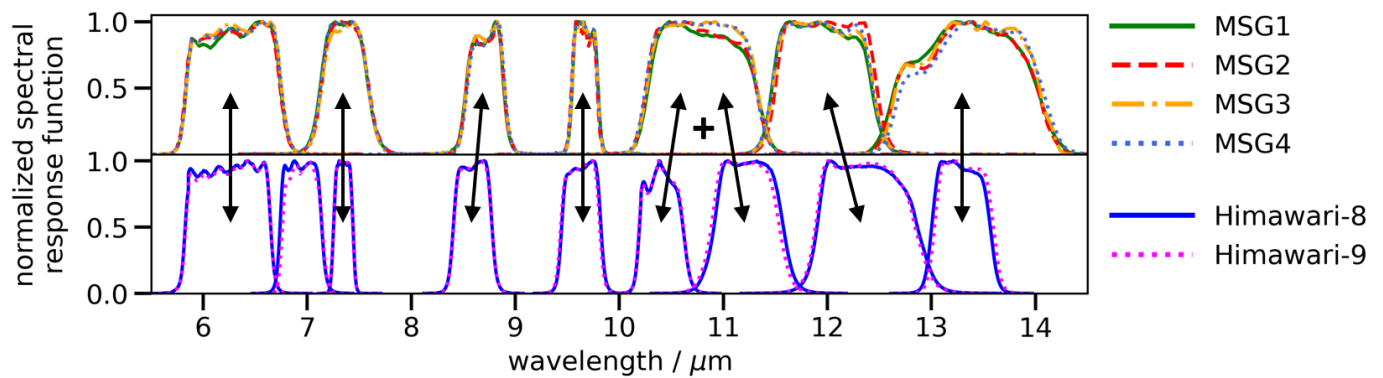


Figure 3. Peak-normalized spectral response functions of different versions of MSG/SEVIRI and Himawari/AHI. The arrows indicate corresponding channels in both instrument, i.e., channels that have approximately the same central wavelengths. In the special case of the MSG/SEVIRI channel at 10.8 μm , two channels at Himawari/AHI are equally close but shifted to the upper and the lower end of the band; thus, the mean of both channels is used for the naive SBAFs instead of Equation (6).

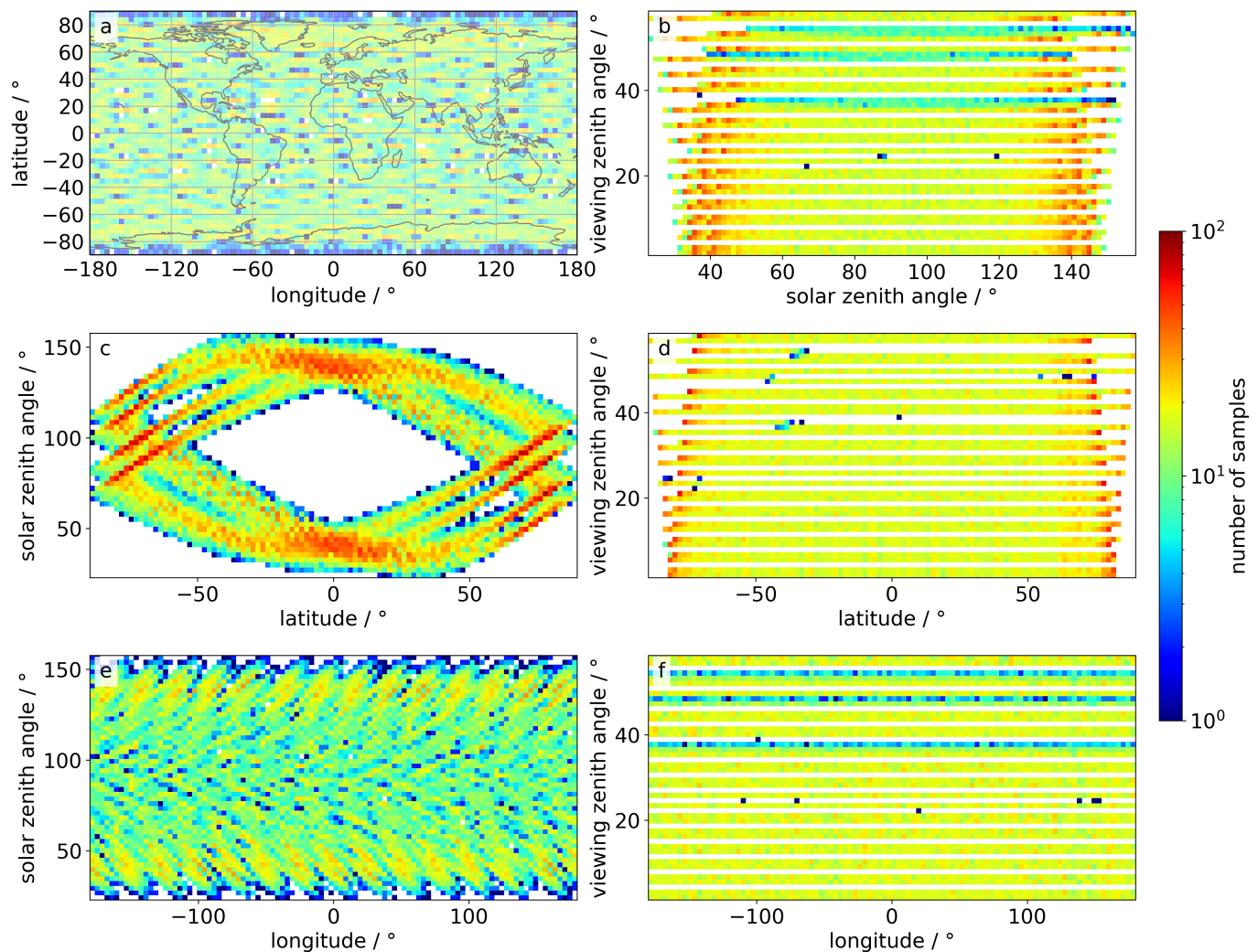


Figure 4. Distribution of the training dataset samples with respect to (a) latitude and longitude, (b) viewing zenith angle and solar zenith angle, (c) solar zenith angle and latitude, (d) viewing zenith angle and latitude, (e) solar zenith angle and longitude, and (f) viewing zenith angle and longitude.

For the collected spectra, the effective radiances of the imagers (MSG2–4/SEVIRI, Himawari-8/AHI, MTG1/FCI) for all thermal infrared channels are derived using parallelized calculations on DLR’s CARA cluster (*Cluster for Advanced Research in Aerospace*). Corresponding equivalent brightness temperatures are derived using look-up tables, which were provided for MSG/SEVIRI [65] and Himawari-8/AHI [66] and additionally calculated for for MTG1/FCI.

2.4.3. Fitting of Polynomials as SBAFs

Eight different types of polynomials are tested as SBAFs (i.e., as function f in Equation (3)). They are fitted to the effective radiances derived from MetOp/IASI spectra (see Section 2.4.2) to change Himawari-8/AHI and MTG1/FCI measurements such that they look like they were measured by MSG2/SEVIRI, or to map two MSG/SEVIRI units (i.e., SEVIRI aboard MSG1–4) to each other. For each pair of instruments and each type of polynomial function, seven functions are fitted corresponding to each of the thermal infrared channels of MSG/SEVIRI. The polynomials in consideration are: the linear function with the corresponding channels directly related to each other; polynomials of 5th degree with one thermal infrared channel as input; polynomials of 5th degree with one thermal infrared channel and the latitude as input; polynomials of 1st to 3rd degree using all thermal infrared channels as input; and polynomials of 1st to 2nd degree using all thermal infrared channels and the latitude as input (see Table 1). As described in Section 2.4.1, there is no clear correspondence for the 10.8 μm channel when mapping Himawari-8/AHI to MSG2/SEVIRI, such that both candidate bands of the former are used; thus, N is increased by one in this particular case (indicated by † in Table 1). Note that these functions have many coefficients, e.g., $N = 9$ and $D = 3$ leads to 220 free parameters.

The fitting of the polynomials minimizes the sum of the squared errors between the target effective radiances and the SBAF-corrected effective radiances. The effective radiances and the coefficients of the polynomials are arranged in a vector equation which is solved using NumPy’s *lstsq* function [67]. Inputs and targets are standardized (i.e., the values are shifted by the mean and then divided by the standard deviation of the corresponding quantity in the training dataset).

Table 1. Polynomials with different numbers of input channels (N) and degrees (D) trained as SBAFs in this study. For the SBAFs mapping Himawari-8/AHI to MSG2/SEVIRI marked by † , the functions use both thermal channels close to 10.8 μm of Himawari-8/AHI to reproduce the 10.8 μm measurement of MSG/SEVIRI, as there is no preferred candidate available. Thus, N is effectively increased by one in these cases.

Himawari-8 to MSG2		MTG1 to MSG2		MSG3 to MSG2		MSG4 to MSG2		MSG4 to MSG3	
N	D	N	D	N	D	N	D	N	D
<i>using one thermal effective radiance as input</i>									
1^\dagger	1	1	1	1	1	1	1	1	1
1^\dagger	5	1	5	1	5	1	5	1	5
<i>using one thermal effective radiance and the latitude as input</i>									
2^\dagger	5	2	5	2	5	2	5	2	5
<i>using all thermal effective radiances as input</i>									
9	1	7	1	7	1	7	1	7	1
9	2	7	2	7	2	7	2	7	2
9	3	7	3	7	3	7	3	7	3
<i>using all thermal effective radiances and the latitude as input</i>									
10	1	8	1	8	1	8	1	8	1
10	2	8	2	8	2	8	2	8	2

3. Results

3.1. Comparison of Different Sets of SBAFs

Table 2 shows the mean and the standard deviation of the difference in equivalent brightness temperatures of different imagers in analog channels as calculated using the

MetOp/IASI-based dataset of spectra described in Section 2.4.2. There are significant systematic biases in the order of 1 K. In the case of Himawari-8/AHI vs. MSG2/SEVIRI, mainly the channels at 9.7, 12.0, and 13.4 μm are affected. For MTG1/FCI vs. MSG2/SEVIRI, the channels at 6.2, 12.0, and 13.4 μm show the largest mean differences in equivalent brightness temperatures. Notably, also different SEVIRI units lead to different equivalent brightness temperatures in the 13.4 μm channel, although the SRFs deviate only weakly from one another (compare Figure 3); in all other SEVIRI channels, the mean differences are in the order of magnitude of the instrumental noise [36].

Table 2. Mean and standard deviation of the difference in the brightness temperatures of different instruments and different channels without application of SBAFs based on convolved MetOp/IASI spectra. In the case of Himawari-8/AHI and MTG1/FCI, the channels analog to the MSG2/SEVIRI bands are selected (except for the MSG2/SEVIRI band centered at 10.8 μm , which has two corresponding channels at Himawari-8/AHI). Results are given in Kelvin.

Channel / μm	Himawari-8 vs. MSG2		MTG1 vs. MSG2		MSG3 vs. MSG2		MSG4 vs. MSG2		MSG4 vs. MSG3	
	Mean	St.dev.	Mean	St.dev.	Mean	St.dev.	Mean	St.dev.	Mean	St.dev.
6.2	−0.28	0.09	1.16	0.38	0.13	0.05	0.12	0.04	−0.01	0.01
7.3	0.09	0.25	0.18	0.39	0.08	0.03	−0.05	0.04	−0.13	0.07
8.7	−0.18	0.28	0.04	0.07	0.00	0.01	0.02	0.03	0.02	0.02
9.7	−0.77	0.36	−0.09	0.06	−0.05	0.03	0.03	0.02	0.08	0.03
10.8	/	/	0.19	0.26	−0.01	0.02	−0.02	0.01	0.00	0.02
12.0	−0.88	0.66	−0.74	0.59	0.07	0.05	0.08	0.07	0.02	0.02
13.4	2.94	1.17	2.56	0.99	−0.36	0.16	−1.40	0.61	−1.04	0.46

Applying the fitted SBAFs easily removes the non-zero means of the imager-pairs in Table 2 (not shown). Thus, it is more interesting to which degree the SBAFs also reduce the standard deviations in the equivalent brightness temperature differences, σ , given in Table 2. Figure 5 shows σ using different SBAFs for different MSG2/SEVIRI channels normalized to the situation without spectral correction. The results indicate that increasing N and D leads to better mappings. As a consequence, the best results are generally given for $N = 9$, $D = 3$ for Himawari-8/AHI to MSG2/SEVIRI, and $N = 7$, $D = 3$ for the mapping of MTG1/FCI to MSG2/SEVIRI as well as mappings between different MSG/SEVIRI units (see Supplementary Material). However, there are also channels where the simple SBAFs work well. The 12.0 and 13.4 μm channels with the largest σ before spectral correction (see Table 2) also belong to the channels with the strongest reduction in σ after applying SBAFs. For both imager pairings, σ of the 13.4 μm channel decreases already by about 60% when using the simplest SBAFs; increasing the complexity of the correction function leads only to minor improvements. For the 12.0 μm channel, σ decreases slower, but in both imager pairings, a significant reduction is observable when the SBAFs include all thermal channels of the initial instrument (i.e., when using $N = 9$, $D = 1$ for Himawari-8/AHI and $N = 7$, $D = 1$ for MTG1/FCI); again, only minor changes are achieved by a higher complexity. However, there are channels which benefit from complex SBAFs: for example, σ of the 8.7 μm channel in the pairing of MTG1/FCI and MSG2/SEVIRI reduces by about 30% when using $N = 7$, $D = 3$ instead of $N = 7$, $D = 1$. The latitude as an additional input feature leads to a reduction of σ (compare $N = 1$, $D = 5$ with $N = 2$, $D = 5$), but the decrease is significantly stronger when using all thermal channels as input instead (i.e., $N = 9$, $D = 1$ and $N = 7$, $D = 1$). Using the latitude in addition to all thermal channels generally does not lead to a notable improvement (e.g., compare $N = 9$, $D = 2$ with $N = 10$, $D = 2$).

Based on these results for the different SBAFs, three different sets are composed, including polynomials of any N and up to $D = 1$ (labeled *fast* from now on), $D = 2$ (*moderate*), and $D = 3$ (*best*). The *moderate* setting will be applied in the following sections.

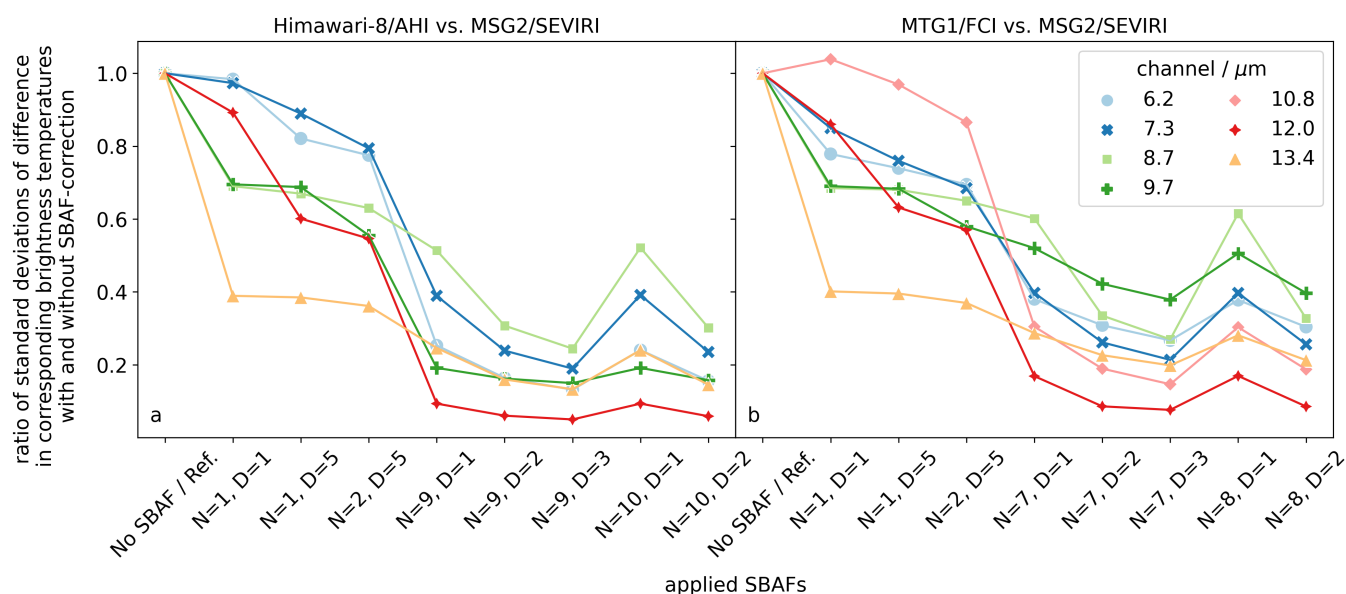


Figure 5. Visualization of the change of the standard deviation of the difference in equivalent brightness temperatures with SBAF-correction with respect to the case without it. Various SBAFs with different numbers of input variables N and degrees D are shown (see Section 2.4.3 for a detailed description). The MSG2/SEVIRI channel is color-coded. (a) shows the comparison of Himawari-8/AHI and (b) of MTG1/FCI with respect to MSG2/SEVIRI, respectively. The $10.8\ \mu\text{m}$ channel is not shown for Himawari-8/AHI as it has two channels which are in the $10.8\ \mu\text{m}$ band for MSG2/SEVIRI, such that no clearly corresponding channel of the Himawari-8/AHI imager can be identified.

3.2. Comparison of Main and Rapid Scan MSG/SEVIRI Units

In Section 2.4.1, it was pointed out that the SRFs of the different MSG/SEVIRI units slightly differ from each other, and the calculations of Section 3.1 showed that these differences have a measurable impact on the equivalent brightness temperatures. Thus, the effect of the SBAFs can be tested using actual collocated observations from different MSG/SEVIRI units. Particularly, the main instrument at 0°E (operational) and the instrument at 9.5°E with limited spatial coverage but higher temporal resolution (rapid scan mode) are used. Two comparisons are performed: in the years 2015–2016, MSG3 was operational with MSG2 in rapid scan mode, whereas in 2019–2020, the satellite MSG4 was operational with MSG3 in rapid scan mode.

As the rapid scan unit covers only the upper third of the SEVIRI disc, the observations are limited to latitudes between 20°N and 65°N with longitudes of $4.75^\circ\text{E} \pm 0.05^\circ$. The chosen longitude ensures that observations are made under similar viewing zenith angles (but still with different azimuth angles). To avoid the impact of small-scale features or slight miscollocation, observations from each satellite are averaged over 3×3 pixels. Only nighttime observations are used, to reduce the impact of azimuthal anisotropy, which is larger during daytime. For the operational satellite, observations from 00:00 UTC are used, whereas for the rapid scan unit, the observations from 00:10 UTC are used. The reason is that SEVIRI measures bottom-up, i.e., starting with southernmost latitudes and proceeding line-by-line towards the northernmost latitudes. Assuming that SEVIRI needs approximately 5 min to cover one third of the SEVIRI disc (in reality it is slightly less), the operational unit starting to measure at 00:00 UTC would reach the upper third only around 00:10 UTC. For each comparison, 12 scenes are used, with one scene for each month. Two corrections are applied to the originally measured effective radiances: first, the so-called re-analysis GSICS calibration corrections are used instead of the default near-realtime corrections. These two versions differ in the latency time until provision as well as the number of collocations with respect to a reference instrument used for their derivation [68]. Second, the moderate SBAFs are used to map the measurements of the operational unit to

the rapid scan unit. Note that when considering the equivalent brightness temperatures, the SBAF-corrected effective radiances are converted to brightness temperatures using the corresponding relations for the target instrument (i.e., the rapid scan instrument).

The resulting error metrics (e.g., median and mean of the equivalent brightness temperature differences of the collocated observations of two MSG/SEVIRI units with and without different corrections) are given in Table 3. For most channels, these metrics show that applying both GSICS- and SBAF-corrections results in smaller deviations in the equivalent brightness temperatures than applying only the GSICS-correction. There remain some channels for which the opposite is true, but the negative effect is small. Remaining median (mean) deviations are $\lesssim 0.22$ K ($\lesssim 0.39$ K). The impact of the SBAFs is largest in the carbon dioxide channel. In the case of MSG3 to MSG2, the median error is reduced from -0.51 K to 0.0 K and in the case of MSG4 to MSG3, it decreases even from -1.35 K to 0.05 K.

Table 3. Differences in the equivalent brightness temperatures between collocated and simultaneous observations of operational and rapid scan MSG/SEVIRI units. Columns 2–4 show the results for MSG3 at 0°E (operational) and MSG2 at 9.5°E (rapid scan mode) with 33,192 samples. Columns 5–7 show the results for MSG4 at 0°E (operational) and MSG3 at 9.5°E (rapid scan) with 33,216 samples. The median, mean, and standard deviation in the difference of equivalent brightness temperatures are given with no corrections applied (*No corr.*), with re-analysis GSICS-corrections applied to both imagers (*GSICS*), and with re-analysis GSICS-corrections applied to both imagers and additionally SBAFs to map the operational imager to the rapid scan unit (*GSICS+SBAFs*). In the latter case, font color and a marker indicate whether the absolute error metrics for *GSICS+SBAFs* are lower (blue, ↘), same (black, →) or larger (red, ↗) than the results for *GSICS*.

Channel/ μm	MSG3 at 0°E, MSG2 at 9.5°E			MSG4 at 0°E, MSG3 at 9.5°E		
	No corr.	GSICS	GSICS+SBAFs	No corr.	GSICS	GSICS+SBAFs
<i>Median of difference/K</i>						
6.2	0.03	0.10	-0.05 ↘	0.11	-0.07	-0.06 ↘
7.3	0.01	0.05	-0.06 ↗	0.03	-0.16	0.03 ↘
8.7	0.04	0.15	0.15 →	0.11	0.22	0.22 →
9.7	0.03	0.01	0.06 ↗	0.29	0.21	0.12 ↘
10.8	0.04	0.08	0.06 ↘	0.09	0.08	0.10 ↗
12.0	0.07	0.09	0.03 ↘	0.04	0.08	0.06 ↘
13.4	-0.35	-0.51	0.00 ↘	-0.58	-1.35	0.05 ↘
<i>Mean of difference/K</i>						
6.2	0.04	0.10	-0.04 ↘	0.11	-0.06	-0.05 ↘
7.3	0.00	0.06	-0.05 ↘	0.04	-0.11	0.06 ↘
8.7	0.03	0.16	0.15 ↘	0.14	0.39	0.39 →
9.7	0.04	0.08	0.14 ↗	0.28	0.31	0.22 ↘
10.8	0.01	0.10	0.09 ↘	0.10	0.14	0.15 ↗
12.0	0.05	0.12	0.06 ↘	0.09	0.11	0.09 ↘
13.4	-0.36	-0.40	0.07 ↘	-0.51	-1.09	0.15 ↘
<i>Standard deviation of difference/K</i>						
6.2	0.27	0.28	0.28 →	0.33	0.34	0.34 →
7.3	0.52	0.58	0.58 →	0.58	0.64	0.63 ↘
8.7	1.08	1.11	1.11 →	1.15	1.26	1.25 ↘
9.7	0.58	0.67	0.67 →	0.65	0.73	0.74 ↗
10.8	1.23	1.25	1.25 →	1.21	1.24	1.24 →
12.0	1.18	1.19	1.19 →	1.20	1.22	1.22 →
13.4	0.69	0.76	0.74 ↘	0.82	1.03	0.84 ↘

3.3. Applying VACOS with SBAFs to Himawari-8/AHI

Next, the SBAFs are used to apply VACOS to Himawari-8/AHI observations of the Raikoke eruption in 2019. Raikoke, part of the Greater Kuril Chain, is a small volcanic island in the northwestern Pacific halfway between Kamchatka and Japan. On 21 June 2019, it started to erupt explosively, emitting large amounts of sulfur dioxide and volcanic ash as high as 10–14 km [69–71]. Prata et al. [71] used an optimal estimation retrieval

for Himawari-8/AHI observations to investigate the spreading of the volcanic ash cloud eastwards over the northern Pacific in the following days, finding volcanic ash clouds with a mass load in the order of 1 g m^{-2} in the stratosphere at heights of 11–13 km as well as in the troposphere at various levels, partly covering underlying water clouds.

VACOS is used to derive the volcanic ash-related optical depth at $10.8 \mu\text{m}$. Then, a mass extinction coefficient at $10.8 \mu\text{m}$ of $200 \text{ m}^2 \text{ kg}^{-1}$ is used as a best guess to convert the optical depth into a volcanic ash mass column concentration [34], and a threshold of 0.1 g m^{-2} to distinguish between ash-free and ash-contaminated pixels. Figure 6a shows the result after using the naive SBAFs between Himawari-8/AHI and MSG2/SEVIRI. Apparently, large areas of the scene show high ash loads and volcanic ash is falsely detected in many regions. Applying the moderate SBAFs (Figure 6b) leads to a much more confined volcanic ash cloud and lower mass column concentrations than for the naive SBAFs.

To check the plausibility of the derived mass loads and the spatial extent of the volcanic ash cloud when using VACOS with moderate SBAFs, the results are compared with an ICON-ART simulation (Figure 6c). The simulation ran on a global grid with an average horizontal grid spacing of $\Delta\bar{x} = 13.2 \text{ km}$. The atmosphere is resolved by 90 vertical levels up to 75 km altitude. The simulation starts on 21 June 2019 at 12:00 UTC with *initialized analysis data* provided by the German weather service (DWD). Hence, the simulation starts 6 h prior to the beginning of the volcanic eruption. In this work, the simulation accounts for secondary aerosol formation of sulfate, physicochemical transformation of aerosol particles, and the interaction of aerosol particles with short- and long-wave radiation. The corresponding simulation setup is extensively described by Muser [72]. This simulation itself was validated against measurements of CALIPSO/CALIOP, the *TROPOspheric Monitoring Instrument* (TROPOMI) and a look-up table-based retrieval using Himawari-8/AHI observations [50,73]. Comparing VACOS with the ICON-ART data shows that the satellite retrieval fits better to the model output when using the moderate SBAFs than after applying the naive SBAFs. For the former, there is a reasonable spatial agreement of the upper two branches of the ash cloud; the lowermost branch is only very weakly indicated by ICON-ART but much more developed in the VACOS results. Comparing the areas in the manually drawn red rectangles leads to mass loads in the same order of magnitude, although ICON-ART produces overall higher mass loads.

Furthermore, 6-hourly retrievals of VACOS after using moderate SBAFs were compared with the ICON-ART results for a time period of 48 h after 22 June 2019, 02:00 UTC (Figure 7). To compare the spatial overlap of the volcanic ash clouds independent of the mass load, the satellite and model data were rearranged on a grid ranging from 40°N – 60°N and 150°E – 171°W with a latitude \times longitude resolution of $0.2^\circ \times 0.3^\circ$, roughly corresponding to $22 \text{ km} \times 22 \text{ km}$ (with some latitudinal dependence). All data points within a grid box are averaged. Next, only the grid boxes with the highest volcanic ash mass load are selected for ICON-ART (all other grid boxes set to ash-free) such that the number of ash-contaminated grid cells according to VACOS and ICON-ART are equal. This selection scheme ensures that the focus is on the most prominent features and removes bias errors [58,74]. Based on the normalized data arrays, the *fraction skill score* (FSS) is calculated using the implementation in pysteps [75]. $FSS(s)$ is defined as

$$FSS(s) = 1 - \frac{\sum_{i=1}^N [O_i(s) - M_i(s)]^2}{\sum_{i=1}^N [O_i^2(s) + M_i^2(s)]} \quad (7)$$

for N points, and $O_i(s)$ and $M_i(s)$ the fractions of volcanic ash contaminated grid cells in the observation and the model data, respectively, within a window of size $s \times s$ in latitude and longitude around a point i . $FSS = 1$ indicates perfect agreement of the datasets, whereas $FSS = 0$ indicates no overlap [58,76]. Again, a threshold of 0.1 g m^{-2} is used, and for s window scales of 3–45 pixels (roughly 66–990 km). The FSS is shown in Figure 7a: the FSS has a value of roughly 0.35–0.55 for the first scene, but increases and stays above 0.5 for $s = 3$ pixels ($\sim 66 \text{ km}$) for 6–36 h.

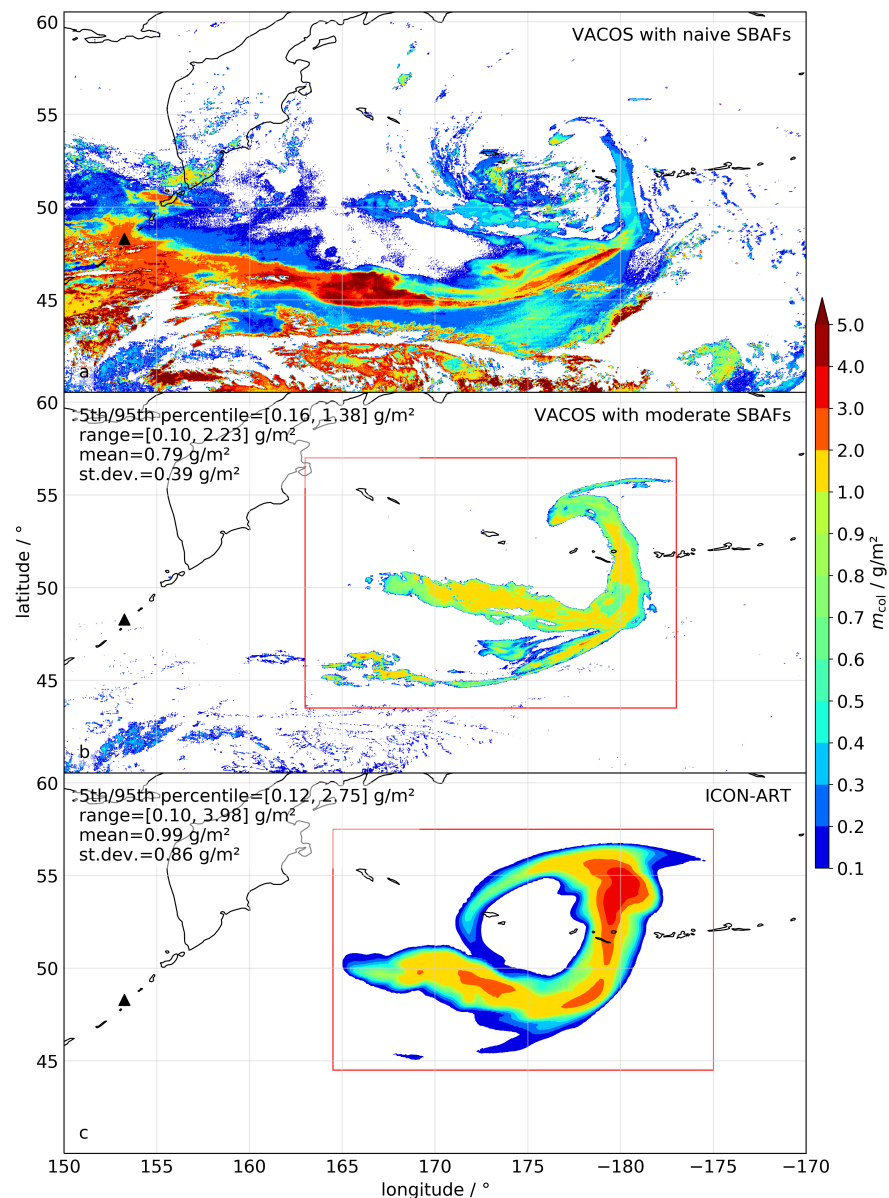


Figure 6. Volcanic ash mass column concentration (m_{col}) for the volcanic ash cloud of the Raikoke volcano at 23 June 2019, 02:00 UTC: VACOS retrieval for Himawari-8/AHI data using (a) naive SBAFs and (b) moderate SBAFs to correct Himawari-8/AHI observations to MSG2/SEVIRI. (c) ICON-ART simulation from Muser [72]. Raikoke volcano is indicated by the black triangle in the lower left corner. Different metrics for the distribution of m_{col} are calculated for the area within the red rectangle and given in the upper left corner.

Figure 7b,c show further metrics (mean, standard deviation, maximum, 5th and 95th percentile) on the quantitative value of the mass load, always derived within a manually defined area encompassing the main volcanic ash cloud (as in Figure 6). For times <12 h, the results for ICON-ART are much larger than for VACOS, indicating that either the model overestimates the mass loads or the satellite retrieval fails at high mass loads close to the vent. However, maxima and means are in good agreement for times ≥ 12 h. Comparing the 5th and the 95th percentiles or the standard deviations for the VACOS and the ICON-ART data indicates that the model produces a larger spread in mass loads than the satellite retrieval.

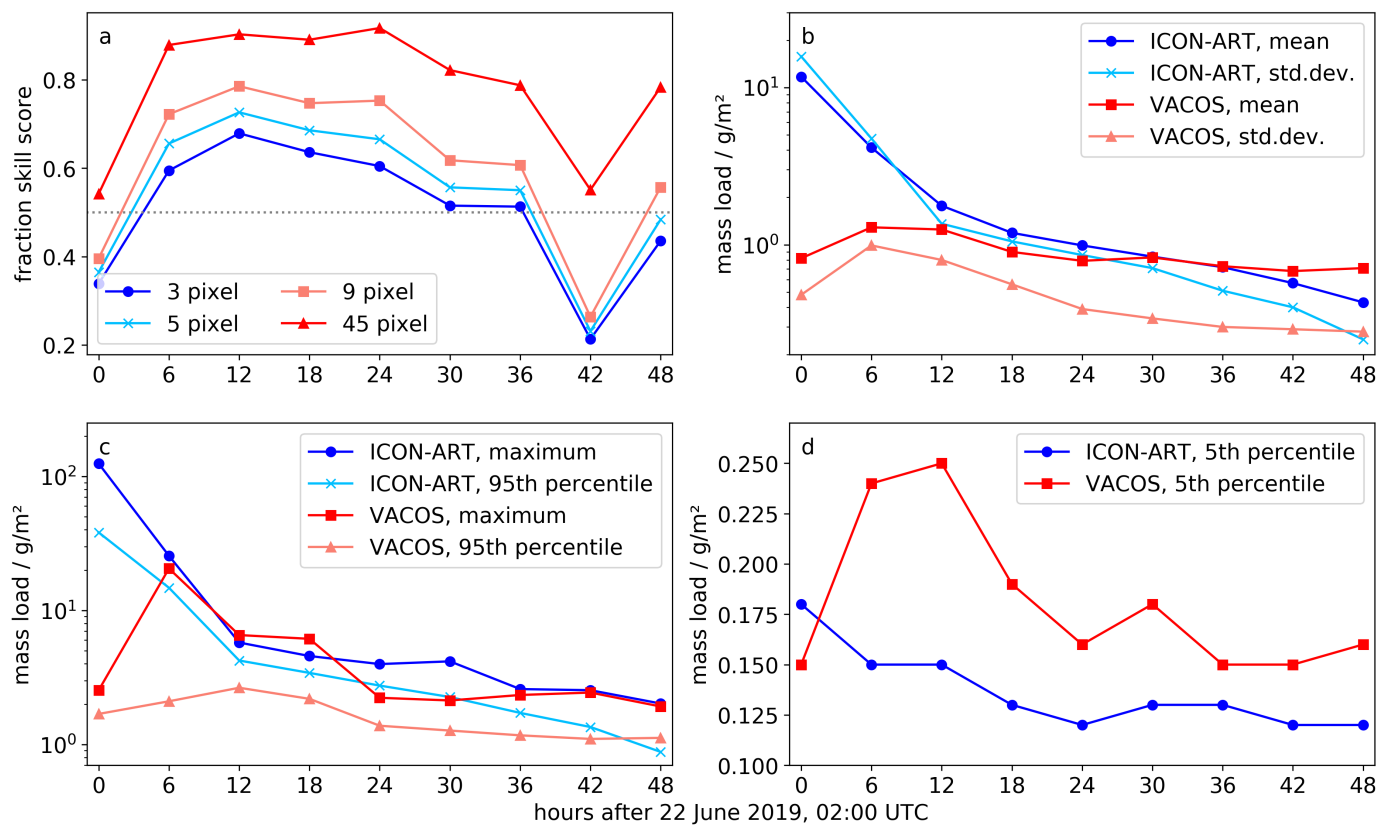


Figure 7. Comparison of volcanic ash cloud data retrieved from VACOS from Himawari-8/AHI using moderate SBAFs and simulated with ICON-ART for the Raikoke eruption from 22 June 2019, 02:00 UTC to 24 June 2019, 02:00 UTC. (a) The fraction skill score using kernels of 3–45 pixels. (b) Mean and standard deviations for the volcanic ash mass loads. (c) Maximum and 95th percentile for the volcanic ash mass loads. (d) The 5th percentile for the volcanic ash mass loads. See text for details.

3.4. Applying CiPS with SBAFs to MTG1/FCI

Now, CiPS is applied to MTG1/FCI mock data and MSG3/SEVIRI observations, both for 20 September 2017 at 12:00 UTC, and both spectrally transferred to MSG2/SEVIRI using moderate SBAFs. The MSG3/SEVIRI data are also re-analysis GSICS-corrected. Figure 8 shows the different CiPS products for the two different satellite datasets. Pixels with a cirrus cloud probability below 0.62 are masked as suggested by Strandgren et al. [15]. CiPS results for both datasets are also shown as two-dimensional histogram. MSG3/SEVIRI-based results were up-sampled to MTG1/FCI resolution using a nearest neighbor algorithm.

The derived cirrus probability is similar for MSG3/SEVIRI and MTG1/FCI and clearly distinguishes cirrus from cirrus-free pixels. However, using MTG1/FCI leads to cirrus probabilities of 0.5–1, whereas using MSG3/SEVIRI produces less samples in the intermediate regime 0.5–0.8. For the ice optical thickness, both satellite datasets lead to comparable results, with the MTG1/FCI-based retrieval slightly underestimating the optical thickness. Especially at high latitudes, there are notable deviations visible for the two satellite datasets. The ice cloud top height retrieval generally produces a very high agreement for both satellites over the full range of available heights (3–18) and at all latitudes. There is a very small fraction of samples (<0.01%) with MTG1/FCI-based ice cloud top heights >20 km, i.e., strong overestimation with respect to the MSG3/SEVIRI-based result. A close inspection of these samples shows that nearly all of them are located at the very edge of the MTG1/FCI disc (not shown).

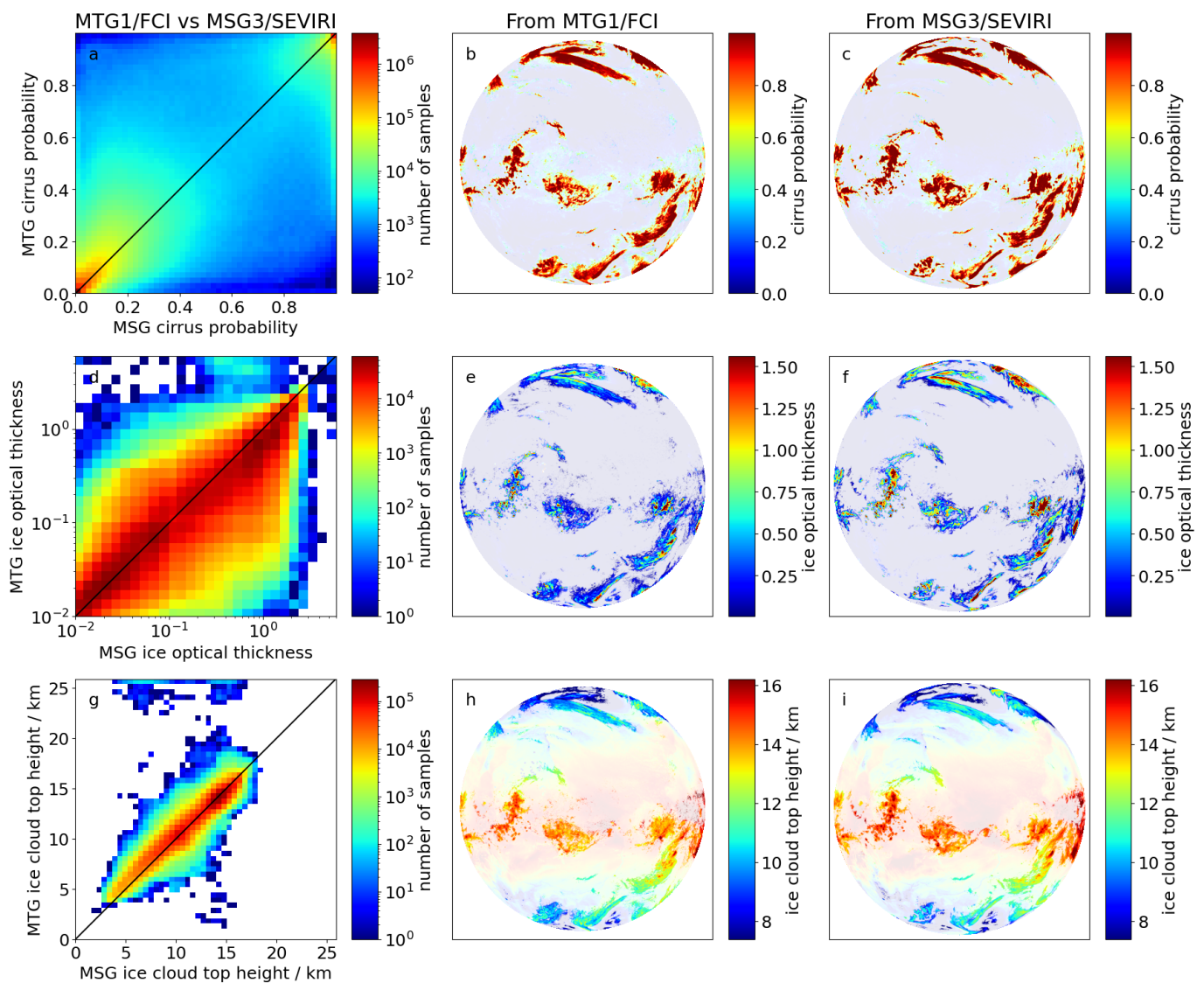


Figure 8. Application of the CiPS retrievals for the (a–c) cirrus probability, (d–f) the ice optical thickness, and (g–i) the ice cloud top height. Results are shown using (b,e,h) MTG1/FCI test data, and (c,f,i) MSG3/SEVIRI observations, both after applying moderate SBAFs with respect to MSG2/SEVIRI and the re-analysis GSICS-correction for MSG3/SEVIRI for a scene on 20 September 2017 at 12:00 UTC. A mask was applied to the satellite images to show only the regions in which the cirrus cloud probability is larger than 0.62. (a,d,g) The CiPS products resulting from both satellite datasets are shown as two-dimensional histogram, with (a) including all pixels whereas (d,g) contain only samples for which the cirrus probability is larger than 0.62 according to both MTG1/FCI and MSG3/SEVIRI.

4. Discussion

The comparison of equivalent brightness temperatures of corresponding channels of different imagers derived from common MetOp/IASI observations (Section 3.1) demonstrated the magnitude of differences in the imager observations. This is particularly true for different imager instruments, e.g., when comparing Himawari-8/AHI or MTG1/FCI with MSG2/SEVIRI. In these cases, the mean and the standard deviation in the brightness temperature differences are in the order of 1–3 K and 1 K, respectively, making spectral corrections necessary. Even the comparison of successive instruments of the same type (MSG/SEVIRI) reveals mean brightness temperature differences >1 K in the 13.4 μm channel; for the remaining thermal infrared channels, mean differences are in the order of the

instrumental noise [36]. Generally, the deviation of the imager measurements is strongly channel-dependent, as the channels, e.g., differ in the variability of their SRFs, their location with respect to the Planck curve and are differently affected by atmospheric clouds, aerosols, and gases. Thus, often, only one or a few channels need to be corrected (e.g., in the case of MSG/SEVIRI, only the 13.4 μm channel must be corrected). The application of SBAFs reduces both the mean and the standard deviation in the brightness temperature difference of two imager observations. The latter experiences reductions of up to 60–90%. Generally, the corrections become better the more complex the SBAFs are (with respect to N and D), presumably because they can better handle nonlinearities between the effective radiances measured for corresponding channels at different imagers and can exploit the possible correlation between channels at different parts of the thermal infrared spectrum. However, the results drawn from Figure 5 allow no inferences to be made as to whether all thermal channels contribute equally to each set of SBAFs or whether specific combinations of thermal infrared channels are more closely linked through the SBAFs than others (e.g., all atmospheric window channels or all water vapor channels). The magnitude of the SBAF-related correction is again channel-dependent: the two considered examples (Himawari-8/AHI and MTG1/FCI compared to MSG2/SEVIRI, respectively) showed that the 13.4 μm channel improves already by 60% when using the simplest SBAFs ($N = 1$, $D = 1$), whereas the 7.3 μm channel improves similarly strong only after applying a correction which exploits all available thermal infrared channels.

The direct comparison of collocated observations of the SEVIRI imager aboard MSG2 to MSG4 (Section 3.2) shows that the brightness temperature differences are on average small and in the same order of magnitude as the instrumental noise [36]. Once again, the only exception is the 13.4 μm channel which shows absolute average biases beyond 0.5 K. This bias can be removed by applying simultaneously the re-analysis GSICS-correction and the SBAFs, whereas the standard deviation of the brightness temperature difference remains unchanged. The results also stress that GSICS-corrections and SBAFs should be applied together. For instance, considering equivalent brightness temperatures for the 13.4 μm channel for MSG4 to MSG3, the median deviation without any correction is -0.58 K and increases to -1.35 K when applying only the GSICS-correction. However, if additionally the SBAFs are applied, it becomes 0.05 K. In some channels, the application of SBAFs and the GSICS-correction does not lead to an improvement with respect to applying only the latter. This might have various causes, including numerical inaccuracies in the SBAFs, the presence of meteorological conditions that deviate strongly from the mean in the MetOp/IASI-based training dataset, or the consideration of night-only scenes in contrast to the mixture of day and night samples in the training dataset.

The application of VACOS to Himawari-8/AHI observations (Section 3.3) demonstrates the necessity as well as the ability of SBAFs. Using VACOS combined with moderate SBAFs allowed the retrieval of the Raikoke 2019 volcanic ash cloud, as shown by a comparison to a well-validated model calculation using ICON-ART. It should be noted that neither dataset represents the truth, as both are subject to uncertainty; instead, their comparison should be viewed as a consistency check. Reasonable spatial agreement was found for times of roughly 6–36 h after the 22 June 2019, 02:00 UTC, and comparable mass loads are found for times ≥ 12 h; both stresses the good performance of the two independent model- and satellite-based methods. Note that the mass loads derived from VACOS depend on the mass extinction coefficient at 10.8 μm , whose value was based on an assumption. Furthermore, VACOS and ICON-ART results deviate quantitatively strongly at early times up to 12 h. Although both datasets could be the cause for this, models generally perform better the shorter the prediction periods are [76], whereas VACOS might underestimate high mass loads as observed close to the vent [56]. Possible reasons are the saturation of the thermal infrared signal for very thick volcanic ash clouds [56], the emission of volcanic gases such as sulfur dioxide leading to an impact on, e.g., the 8.7 μm channel [11], or the presence of water and ice clouds that might affect the strength of the volcanic ash signal or hide it altogether due to their contrary signature in the thermal infrared atmospheric window [77,78].

The application of CiPS to synthetic MTG1/FCI observations as well as to MSG3/SEVIRI data using SBAFs produced comparable results for the cirrus probability and the ice cloud top height (Section 3.4). However, the CiPS ice cloud top height retrieval depends more heavily on the latitude than on the satellite brightness temperatures as was shown by Strandgren et al. [59] when analyzing the importance of the individual input features of CiPS; this is in strong contrast to the remaining CiPS products. This notable latitudinal dependence could explain the high agreement of the ice cloud top height retrievals for both satellite datasets. The ice optical thickness retrieval leads to underestimations when using MTG1/FCI data. Although this underestimation might be a shortcoming of the retrieval, it might also be explained by inaccuracies in the MTG1/FCI test data, e.g., due to the plane parallel radiative transfer simulations [41] and the selection of ice cloud optical property models in RTTOV or due to the input cloud properties. These limitations in the MTG1/FCI mock data as well as the extremely slant observation geometry also provide explanations for the strong overestimation of the MTG1/FCI-derived ice cloud top heights at the very edge of the MTG1/FCI disc. Thus, the retrieval setup (i.e., CiPS with SBAFs) should be further tested as soon as actual MTG1/FCI observations become available. As MSG4/SEVIRI is expected to be still operational when MTG1/FCI becomes active, a direct comparison as demonstrated in this work for MSG will be possible for those two imagers.

5. Conclusions

The present study aimed to develop and test a new set of spectral band adjustment factors (SBAFs) to correct thermal measurements from geostationary imagers for differences in instrument-specific spectral characteristics. In particular, the SEVIRI imagers aboard MSG2 to MSG4, Himawari-8/AHI, and the upcoming MTG1/FCI instrument were considered. The SBAFs were determined using imager effective radiances derived for common MetOp/IASI hyperspectral measurements. The correction functions were separate polynomials for each band of the target imager. As a novelty, polynomials using all thermal channels of the original instrument were considered, as well as polynomials with degrees up to fifth order. Using the IASI-based imager-equivalent brightness temperatures, it was found that their mean differences between corresponding channels of different instruments can be >1 K but are channel-dependent. The differences can be significantly reduced using SBAFs, with more complex SBAFs leading to better results; again, this was shown to be channel-dependent. Using observations of collocated MSG/SEVIRI measurements from the operational and the rapid-scan unit, the effect of the SBAFs was demonstrated, with the largest impact and necessity in the 13.4 μm channel. It was highlighted that the SBAFs should be combined with the re-analysis GSICS-corrections if possible. The SBAFs were applied in combination with the volcanic ash retrieval VACOS and the ice cloud retrieval CiPS. VACOS with SBAFs was applied to Himawari-8/AHI observations of the Raikoke eruption in the Northern Pacific in 2019 and compared to an ICON-ART simulation, which showed good spatial agreement (e.g., a fraction skill score >0.5 for a spatial resolution of approximately 66 km) between 6 and 36 h after the 22 June 2019, 02:00 UTC. CiPS with SBAFs was applied to simulated MTG1/FCI test data and compared to retrievals based on MSG3/SEVIRI observations, showing similar results for the ice cloud probability and top height, but underestimations for the ice optical thickness.

In future work, the technique could be improved by further cleaning the training dataset of the SBAFs with respect to cases with limited occurrence; one example is sunglint effects which can cause increases of the equivalent brightness temperatures in the order of 0.01–0.1 K even in the thermal infrared atmospheric window channels [79]. In addition, more specialized subsets of the full training dataset could be used, e.g., for specific latitudes, surface types, or times of the day, since the exact form of the target spectrum is crucial [17]. Doing so would allow to adjust each pixel with a special correction function. An extension to the visible spectrum would require a different dataset than the MetOp/IASI measurements. The SBAFs could be compared to similar studies, e.g., by Scarino et al. [19], and the

technique could be applied to other imagers such as ABI aboard GOES16 and GOES17, enabling retrievals on the full geostationary ring.

To conclude, this work explored a method to apply existing satellite retrievals to all available and upcoming geostationary imagers with the goal to reach a nearly-global coverage.

Supplementary Materials: The following supporting information can be downloaded at: <https://www.mdpi.com/article/10.3390/rs15051247/s1>, File S1: metrics of the spectral band adjustment factors; File S2: Python scripts to apply the spectral band adjustment factors; File S3: dependencies of the imager observations.

Author Contributions: Conceptualization, D.P. and L.B.; methodology, D.P.; software, D.P.; validation, D.P.; formal analysis, D.P.; investigation, D.P.; data sources, L.M.; data curation, D.P.; writing—original draft preparation, D.P.; writing—review and editing, L.B., R.M., M.J. and L.M.; visualization, D.P.; supervision, L.B., R.M. and M.J.; project administration, L.B., R.M. and M.J.; funding acquisition, D.P., L.B., R.M. and M.J. All authors have read and agreed to the published version of the manuscript.

Funding: Parts of the work on which this publication is based was carried out on behalf of the German weather service (Deutscher Wetterdienst, DWD) within the projects VA-ICE-2020 and M-ICE-2022.

Data Availability Statement: Data presented in this study are available upon request from the corresponding author and as supplementary material.

Acknowledgments: The MSG/SEVIRI and MetOp/IASI data were provided by EUMETSAT (European Organisation for the Exploitation of Meteorological Satellites). Himawari-8/AHI measurements were provided by JAXA (Japan Aerospace Exploration Agency). Calculations were partly executed on DLR's CARA (Deutsches Zentrum für Luft- und Raumfahrt; Cluster for Advanced Research in Aerospace). Furthermore, we like to thank C. Voigt and T. Bülle for constructive discussions and two reviewers for the helpful comments to improve the manuscript.

Conflicts of Interest: The authors declare no conflicts of interest.

Abbreviations

The most frequently used abbreviations in this manuscript:

AHI	Advanced Himawari Imager
CiPS	Cirrus Properties from SEVIRI
DLR	Deutsches Zentrum für Luft- und Raumfahrt
DWD	Deutscher Wetterdienst
FCI	Flexible Combined Imager
FSS	Fraction Skill Score
GSICS	Global Space-based Inter-Calibration System
IASI	Infrared Atmospheric Sounding Interferometer
ICON-ART	Icosahedral Nonhydrostatic model-Aerosols and Reactive Trace gases
MetOp	Meteorological Operational satellite
MSG	Meteosat Second Generation
MTG	Meteosat Third Generation
SBAF	Spectral Band Adjustment Factor
SEVIRI	Spinning Enhanced Visible and InfraRed Imager
SRF	Spectral Response Function
VACOS	Volcanic Ash Cloud properties Obtained from SEVIRI

References

- Schmetz, J.; Pili, P.; Tjemkes, S.; Just, D.; Kerkmann, J.; Rota, S.; Ratier, A. An Introduction to Meteosat Second Generation (MSG). *Bull. Am. Meteorol. Soc.* **2002**, *83*, 977–992. [[CrossRef](#)]
- Schmit, T.J.; Gunshor, M.M.; Menzel, W.P.; Gurka, J.J.; Li, J.; Bachmeier, A.S. Introducing the Next-Generation Advanced Baseline Imager on GOES-R. *Bull. Am. Meteorol. Soc.* **2005**, *86*, 1079–1096. [[CrossRef](#)]
- Schmit, T.J.; Griffith, P.; Gunshor, M.M.; Daniels, J.M.; Goodman, S.J.; Leblair, W.J. A Closer Look at the ABI on the GOES-R Series. *Bull. Am. Meteorol. Soc.* **2017**, *98*, 681–698. [[CrossRef](#)]

4. Bessho, K.; Date, K.; Hayashi, M.; Ikeda, A.; Imai, T.; Inoue, H.; Kumagai, Y.; Miyakawa, T.; Murata, H.; Ohno, T.; et al. An Introduction to Himawari-8/9—Japan’s New-Generation Geostationary Meteorological Satellites. *J. Meteorol. Soc. Jpn.* **2016**, *94*, 151–183. [[CrossRef](#)]
5. Yang, J.; Zhang, Z.; Wei, C.; Lu, F.; Guo, Q. Introducing the New Generation of Chinese Geostationary Weather Satellites, Fengyun-4. *Bull. Am. Meteorol. Soc.* **2017**, *98*, 1637–1658. [[CrossRef](#)]
6. Durand, Y.; Hallibert, P.; Wilson, M.; Lekouara, M.; Grabarnik, S.; Aminou, D.; Blythe, P.; Napierala, B.; Canaud, J.L.; Pigouche, O.; et al. The flexible combined imager onboard MTG: From design to calibration. In Proceedings of the Sensors, Systems, and Next-Generation Satellites XIX, Toulouse, France, 21–24 September 2015; Meynart, R., Neeck, S.P., Shimoda, H., Eds.; International Society for Optics and Photonics, SPIE: Bellingham, WA, USA: 2015; Volume 9639, pp. 1–14. [[CrossRef](#)]
7. Francis, P.N.; Cooke, M.C.; Saunders, R.W. Retrieval of physical properties of volcanic ash using Meteosat: A case study from the 2010 Eyjafjallajökull eruption. *J. Geophys. Res. Atmos.* **2012**, *117*. [[CrossRef](#)]
8. Gouhier, M.; Deslandes, M.; Guéhenneux, Y.; Hereil, P.; Cacaault, P.; Josse, B. Operational Response to Volcanic Ash Risks Using HOTVOLC Satellite-Based System and MOCAGE-Accident Model at the Toulouse VAAC. *Atmosphere* **2020**, *11*, 864. [[CrossRef](#)]
9. Prata, A.J.; Grant, I.F. Retrieval of microphysical and morphological properties of volcanic ash plumes from satellite data: Application to Mt Ruapehu, New Zealand. *Q. J. R. Meteorol. Soc.* **2001**, *127*, 2153–2179. [[CrossRef](#)]
10. Prata, A.J.; Prata, A.T. Eyjafjallajökull volcanic ash concentrations determined using Spin Enhanced Visible and Infrared Imager measurements. *J. Geophys. Res. Atmos.* **2012**, *117*. [[CrossRef](#)]
11. Gray, T.M.; Bennartz, R. Automatic volcanic ash detection from MODIS observations using a back-propagation neural network. *Atmos. Meas. Tech.* **2015**, *8*, 5089–5097. [[CrossRef](#)]
12. Piscini, A.; Picchiani, M.; Chini, M.; Corradini, S.; Merucci, L.; Del Frate, F.; Stramondo, S. A neural network approach for the simultaneous retrieval of volcanic ash parameters and SO₂ using MODIS data. *Atmos. Meas. Tech.* **2014**, *7*, 4023–4047. [[CrossRef](#)]
13. Kox, S.; Bugliaro, L.; Ostler, A. Retrieval of cirrus cloud optical thickness and top altitude from geostationary remote sensing. *Atmos. Meas. Tech.* **2014**, *7*, 3233–3246. [[CrossRef](#)]
14. Bugliaro, L.; Piontek, D.; Kox, S.; Schmidl, M.; Mayer, B.; Müller, R.; Vázquez-Navarro, M.; Peters, D.M.; Grainger, R.G.; Gasteiger, J.; et al. VADUGS: A neural network for the remote sensing of volcanic ash with MSG/SEVIRI trained with synthetic thermal satellite observations simulated with a radiative transfer model. *Nat. Hazards Earth Syst. Sci.* **2022**, *22*, 1029–1054. [[CrossRef](#)]
15. Strandgren, J.; Bugliaro, L.; Sehnke, F.; Schröder, L. Cirrus cloud retrieval with MSG/SEVIRI using artificial neural networks. *Atmos. Meas. Tech.* **2017**, *10*, 3547–3573. [[CrossRef](#)]
16. Zhu, W.; Zhu, L.; Li, J.; Sun, H. Retrieving volcanic ash top height through combined polar orbit active and geostationary passive remote sensing data. *Remote Sens.* **2020**, *12*, 953. [[CrossRef](#)]
17. Chander, G.; Mishra, N.; Helder, D.L.; Aaron, D.B.; Angal, A.; Choi, T.; Xiong, X.; Doelling, D.R. Applications of Spectral Band Adjustment Factors (SBAF) for Cross-Calibration. *IEEE Trans. Geosci. Remote Sens.* **2013**, *51*, 1267–1281. [[CrossRef](#)]
18. Doelling, D.R.; Lukashin, C.; Minnis, P.; Scarino, B.; Morstad, D. Spectral Reflectance Corrections for Satellite Intercalibrations Using SCIAMACHY Data. *IEEE Geosci. Remote Sens. Lett.* **2012**, *9*, 119–123. [[CrossRef](#)]
19. Scarino, B.R.; Doelling, D.R.; Minnis, P.; Gopalan, A.; Chee, T.; Bhatt, R.; Lukashin, C.; Haney, C. A Web-Based Tool for Calculating Spectral Band Difference Adjustment Factors Derived From SCIAMACHY Hyperspectral Data. *IEEE Trans. Geosci. Remote Sens.* **2016**, *54*, 2529–2542. [[CrossRef](#)]
20. Scarino, B.; Doelling, D.R.; Gopalan, A.; Chee, T.; Bhatt, R.; Haney, C. Enhancements to the open access spectral band adjustment factor online calculation tool for visible channels. In Proceedings of the Earth Observing Systems XXIII, San Diego, CA, USA, 19–23 August 2018; Butler, J.J., Xiong, X.J., Gu, X., Eds.; International Society for Optics and Photonics, SPIE: Bellingham, WA, USA: 2018; Volume 10764, pp. 383–396. [[CrossRef](#)]
21. Bhatt, R.; Doelling, D.R.; Scarino, B.; Gopalan, A.; Chee, T.; Haney, C. NASA LaRC Spectral Band Adjustment Factor (SBAF) Online Calculation Tool Update. In Proceedings of the Presentation at the GSICS Annual Meeting 2019, Frascati, Italy, 4–8 March 2019. Available online: http://gsics.atmos.umd.edu/pub/Development/AnnualMeeting2019/4q_SBAF_Update_GSICS_2019_Bhatt.pdf (accessed on 23 January 2023).
22. Qin, Y.; McVicar, T.R. Spectral band unification and inter-calibration of Himawari AHI with MODIS and VIIRS: Constructing virtual dual-view remote sensors from geostationary and low-Earth-orbiting sensors. *Remote Sens. Environ.* **2018**, *209*, 540–550. [[CrossRef](#)]
23. Gunshor, M.M.; Schmit, T.J.; Menzel, W.P.; Tobin, D.C. Intercalibration of Broadband Geostationary Imagers Using AIRS. *J. Atmos. Ocean. Technol.* **2009**, *26*, 746–758. [[CrossRef](#)]
24. Hewison, T.J.; Wu, X.; Yu, F.; Tahara, Y.; Hu, X.; Kim, D.; Koenig, M. GSICS Inter-Calibration of Infrared Channels of Geostationary Imagers Using Metop/IASI. *IEEE Trans. Geosci. Remote Sens.* **2013**, *51*, 1160–1170. [[CrossRef](#)]
25. Minnis, P.; Gambheer, A.V.; Doelling, D.R. Azimuthal anisotropy of longwave and infrared window radiances from the Clouds and the Earth’s Radiant Energy System on the Tropical Rainfall Measuring Mission and Terra satellites. *J. Geophys. Res. Atmos.* **2004**, *109*, 1–13. [[CrossRef](#)]
26. Chander, G.; Hewison, T.J.; Fox, N.; Wu, X.; Xiong, X.; Blackwell, W.J. Overview of Intercalibration of Satellite Instruments. *IEEE Trans. Geosci. Remote Sens.* **2013**, *51*, 1056–1080. [[CrossRef](#)]
27. Jiang, G.; Li, Z. Cross-calibration of MSG1-SEVIRI infrared channels with Terra-MODIS channels. *Int. J. Remote Sens.* **2009**, *30*, 753–769. [[CrossRef](#)]

28. Gunshor, M.M.; Schmit, T.J.; Menzel, W.P. Intercalibration of the Infrared Window and Water Vapor Channels on Operational Geostationary Environmental Satellites Using a Single Polar-Orbiting Satellite. *J. Atmos. Ocean. Technol.* **2004**, *21*, 61–68. [CrossRef]
29. Doelling, D.R.; Haney, C.O.; Scarino, B.R.; Gopalan, A.; Bhatt, R. Improvements to the Geostationary Visible Imager Ray-Matching Calibration Algorithm for CERES Edition 4. *J. Atmos. Ocean. Technol.* **2016**, *33*, 2679–2698. [CrossRef]
30. Rublev, A.N.; Gorbarenko, E.V.; Golomolzin, V.V.; Borisov, E.Y.; Kiseleva, J.V.; Gektin, Y.M.; Zaitsev, A.A. Inter-calibration of Infrared Channels of Geostationary Meteorological Satellite Imagers. *Front. Environ. Sci.* **2018**, *6*, 142. [CrossRef]
31. Govaerts, Y.M.; Rührich, F.; John, V.O.; Quast, R. Climate Data Records from Meteosat First Generation Part I: Simulation of Accurate Top-of-Atmosphere Spectral Radiance over Pseudo-Invariant Calibration Sites for the Retrieval of the In-Flight Visible Spectral Response. *Remote Sens.* **2018**, *10*, 1959. [CrossRef]
32. Quast, R.; Giering, R.; Govaerts, Y.; Rührich, F.; Roebeling, R. Climate Data Records from Meteosat First Generation Part II: Retrieval of the In-Flight Visible Spectral Response. *Remote Sens.* **2019**, *11*, 480. [CrossRef]
33. Xu, N.; Wu, P.; Ma, G.; Hu, Q.; Hu, X.; Wu, R.; Wang, Y.; Xu, H.; Chen, L.; Zhang, P. In-Flight Spectral Response Function Retrieval of a Multispectral Radiometer Based on the Functional Data Analysis Technique. *IEEE Trans. Geosci. Remote Sens.* **2021**, *60*, 1–10. [CrossRef]
34. Piontek, D.; Bugliaro, L.; Schmidl, M.; Zhou, D.K.; Voigt, C. The New Volcanic Ash Satellite Retrieval VACOS Using MSG/SEVIRI and Artificial Neural Networks: 1. Development. *Remote Sens.* **2021**, *13*, 3112. [CrossRef]
35. The Conversion from Effective Radiances to Equivalent Brightness Temperatures. European Organisation for the Exploitation of Meteorological Satellites. 2012. Available online: https://www-cdn.eumetsat.int/files/2020-04/pdf_effect_rad_to_brightness.pdf (accessed on 17 November 2021).
36. Typical Radiometric Noise, Calibration Bias and Stability for Meteosat-8, -9, -10 and -11 SEVIRI. European Organisation for the Exploitation of Meteorological Satellites. 2019. Available online: https://www-cdn.eumetsat.int/files/2020-04/pdf_typ_radiomet_acc_msg-1-2.pdf (accessed on 17 November 2021).
37. Spectral Response Functions (SRFs) and MW Passbands. European Organisation for the Exploitation of Meteorological Satellites, Numerical Weather Prediction Satellite Application Facility. Available online: <https://nwp-saf.eumetsat.int/site/software/rtov/download/coefficients/spectral-response-functions> (accessed on 17 November 2021).
38. Meteosat Series. European Organisation for the Exploitation of Meteorological Satellites. Available online: <https://www.eumetsat.int/our-satellites/meteosat-series> (accessed on 3 November 2022).
39. List of All Satellites. World Meteorological Organization, Observing Systems Capability Analysis and Review Tool. Available online: <https://www.wmo-sat.info/oscar/satellites/> (accessed on 16 November 2021).
40. Holmlund, K.; Grandell, J.; Schmetz, J.; Stuhlmann, R.; Bojkov, B.; Munro, R.; Lekouara, M.; Coppens, D.; Viticchie, B.; August, T.; et al. Meteosat Third Generation (MTG): Continuation and Innovation of Observations from Geostationary Orbit. *Bull. Am. Meteorol. Soc.* **2021**, *102*, E990–E1015. [CrossRef]
41. MTGTD-360 Spectrally Representative FCI L1C Test Products - Package Description. European Organisation for the Exploitation of Meteorological Satellites. 2022. Available online: [https://sftf.eumetsat.int/public/folder/UsCVknVOOkSyCdgpMimJNQ/User-Materials/Test-Data/MTG/MTG_FCI_L1C_SpectrallyRepresentative_TD-360_May2022/MTGTD-360%20Spectrally%20Representative%20FCI%20L1C%20Test%20Products%20-%20Package%20Description%20\(1290888%20V1\).pdf](https://sftf.eumetsat.int/public/folder/UsCVknVOOkSyCdgpMimJNQ/User-Materials/Test-Data/MTG/MTG_FCI_L1C_SpectrallyRepresentative_TD-360_May2022/MTGTD-360%20Spectrally%20Representative%20FCI%20L1C%20Test%20Products%20-%20Package%20Description%20(1290888%20V1).pdf) (accessed on 9 September 2022).
42. GEO-KOMPSAT-2A User Readiness Planning. Korea Meteorological Administration, National Meteorological Satellite Center. Available online: <https://nmsc.kma.go.kr/enhome/html/base/cmm/selectPage.do?page=satellite.gk2a.userReadinessInformation> (accessed on 16 November 2021).
43. Advanced Baseline Imager Solutions. L3Harris. Available online: <https://www.l3harris.com/all-capabilities/advanced-baseline-imager-solutions> (accessed on 17 November 2021).
44. Switchover of the Operational Satellite. Japan Meteorological Agency, Meteorological Satellite Center. Available online: <https://www.data.jma.go.jp/mscweb/en/oper/switchover.html> (accessed on 3 January 2023).
45. Hilton, F.; Armante, R.; August, T.; Barnet, C.; Bouchard, A.; Camy-Peyret, C.; Capelle, V.; Clarisse, L.; Clerbaux, C.; Coheur, P.F.; et al. Hyperspectral Earth Observation from IASI: Five Years of Accomplishments. *Bull. Am. Meteorol. Soc.* **2012**, *93*, 347–370. [CrossRef]
46. Zängl, G.; Reinert, D.; Rípodas, P.; Baldauf, M. The ICON (ICOsahedral Non-hydrostatic) modelling framework of DWD and MPI-M: Description of the non-hydrostatic dynamical core. *Q. J. Roy. Meteor. Soc.* **2015**, *141*, 563–579. [CrossRef]
47. Rieger, D.; Bangert, M.; Bischoff-Gauss, I.; Förstner, J.; Lundgren, K.; Reinert, D.; Schröter, J.; Vogel, H.; Zängl, G.; Ruhnke, R.; et al. ICON-ART 1.0 – a new online-coupled model system from the global to regional scale. *Geosci. Model Dev.* **2015**, *8*, 1659–1676. [CrossRef]
48. Weimer, M.; Schröter, J.; Eckstein, J.; Deetz, K.; Neumaier, M.; Fischbeck, G.; Hu, L.; Millet, D.B.; Rieger, D.; Vogel, H.; et al. An emission module for ICON-ART 2.0: Implementation and simulations of acetone. *Geosci. Model Dev.* **2017**, *10*, 2471–2494. [CrossRef]
49. Schröter, J.; Rieger, D.; Stassen, C.; Vogel, H.; Weimer, M.; Werchner, S.; Förstner, J.; Prill, F.; Reinert, D.; Zängl, G.; et al. ICON-ART 2.1: A flexible tracer framework and its application for composition studies in numerical weather forecasting and climate simulations. *Geosci. Model Dev.* **2018**, *11*, 4043–4068. [CrossRef]

50. Muser, L.O.; Hoshyaripour, G.A.; Bruckert, J.; Horváth, A.; Malinina, E.; Wallis, S.; Prata, F.J.; Rozanov, A.; von Savigny, C.; Vogel, H.; et al. Particle aging and aerosol–radiation interaction affect volcanic plume dispersion: Evidence from the Raikoke 2019 eruption. *Atmos. Chem. Phys.* **2020**, *20*, 15015–15036. [[CrossRef](#)]
51. Giorgetta, M.A.; Brokopf, R.; Crueger, T.; Esch, M.; Fiedler, S.; Helmert, J.; Hohenegger, C.; Kornblueh, L.; Köhler, M.; Manzini, E.; et al. ICON-A, the Atmosphere Component of the ICON Earth System Model: I. Model Description. *J. Adv. Model. Earth Syst.* **2018**, *10*, 1613–1637. [[CrossRef](#)]
52. Heinze, R.; Dipankar, A.; Henken, C.C.; Moseley, C.; Sourdeval, O.; Trömel, S.; Xie, X.; Adamidis, P.; Ament, F.; Baars, H.; et al. Large-eddy simulations over Germany using ICON: A comprehensive evaluation. *Quarterly J. R. Meteorol. Soc.* **2017**, *143*, 69–100. [[CrossRef](#)]
53. Reed, B.E.; Peters, D.M.; McPheat, R.; Grainger, R.G. The Complex Refractive Index of Volcanic Ash Aerosol Retrieved From Spectral Mass Extinction. *J. Geophys. Res. Atmos.* **2018**, *123*, 1339–1350. [[CrossRef](#)]
54. Deguine, A.; Petitprez, D.; Clarisse, L.; Guðmundsson, S.; Outes, V.; Villarosa, G.; Herbin, H. Complex refractive index of volcanic ash aerosol in the infrared, visible, and ultraviolet. *Appl. Opt.* **2020**, *59*, 884–895. [[CrossRef](#)] [[PubMed](#)]
55. Piontek, D.; Hornby, A.; Voigt, C.; Bugliaro, L.; Gasteiger, J. Determination of complex refractive indices and optical properties of volcanic ashes in the thermal infrared based on generic petrological compositions. *J. Volcanol. Geotherm. Res.* **2021**, *411*, 107174. [[CrossRef](#)]
56. Piontek, D.; Bugliaro, L.; Kar, J.; Schumann, U.; Marengo, F.; Plu, M.; Voigt, C. The New Volcanic Ash Satellite Retrieval VACOS Using MSG/SEVIRI and Artificial Neural Networks: 2. Validation. *Remote Sens.* **2021**, *13*, 3128. [[CrossRef](#)]
57. Plu, M.; Bigeard, G.; Sič, B.; Emili, E.; Bugliaro, L.; El Amraoui, L.; Guth, J.; Josse, B.; Mona, L.; Piontek, D. Modelling the volcanic ash plume from Eyjafjallajökull eruption (May 2010) over Europe: Evaluation of the benefit of source term improvements and of the assimilation of aerosol measurements. *Nat. Hazards Earth Syst. Sci.* **2021**, *21*, 3731–3747. [[CrossRef](#)]
58. Plu, M.; Scherllin-Pirscher, B.; Arnold Arias, D.; Baro, R.; Bigeard, G.; Bugliaro, L.; Carvalho, A.; El Amraoui, L.; Eschbacher, K.; Hirtl, M.; et al. An ensemble of state-of-the-art ash dispersion models: Towards probabilistic forecasts to increase the resilience of air traffic against volcanic eruptions. *Nat. Hazards Earth Syst. Sci.* **2021**, *21*, 2973–2992. [[CrossRef](#)]
59. Strandgren, J.; Fricker, J.; Bugliaro, L. Characterisation of the artificial neural network CiPS for cirrus cloud remote sensing with MSG/SEVIRI. *Atmos. Meas. Tech.* **2017**, *10*, 4317–4339. [[CrossRef](#)]
60. Rybka, H.; Burkhardt, U.; Köhler, M.; Arka, I.; Bugliaro, L.; Görsdorf, U.; Horváth, A.; Meyer, C.I.; Reichardt, J.; Seifert, A.; et al. The behavior of high-CAPE (convective available potential energy) summer convection in large-domain large-eddy simulations with ICON. *Atmos. Chem. Phys.* **2021**, *21*, 4285–4318. [[CrossRef](#)]
61. Schumann, U.; Bugliaro, L.; Dörnbrack, A.; Baumann, R.; Voigt, C. Aviation Contrail Cirrus and Radiative Forcing Over Europe During 6 Months of COVID-19. *Geophys. Res. Lett.* **2021**, *48*, e2021GL092771. [[CrossRef](#)]
62. Wang, Z.; Bugliaro, L.; Jurkat-Witschas, T.; Heller, R.; Burkhardt, U.; Ziereis, H.; Dekoutsidis, G.; Wirth, M.; Groß, S.; Kirschler, S.; et al. Observations of microphysical properties and radiative effects of a contrail cirrus outbreak over the North Atlantic. *Atmos. Chem. Phys.* **2023**, *23*, 1941–1961. [[CrossRef](#)]
63. The SEVIRI Instrument. European Organisation for the Exploitation of Meteorological Satellites. 2000. Available online: <https://www.eumetsat.int/media/8161> (accessed on 3 November 2022).
64. Schmetz, J.; Pili, P.; Tjemkes, S.; Just, D.; Kerkmann, J.; Rota, S.; Ratier, A. SEVIRI Calibration. *Bull. Am. Meteorol. Soc.* **2002**, *83*, ES52–ES53. [[CrossRef](#)]
65. Effective Radiance and Brightness Temperature Relation Tables for Meteosat Second Generation. Available online: <https://www.eumetsat.int/media/38301> (accessed on 8 September 2022).
66. Himawari-8 HRIT Data Calibration Table. http://ds.data.jma.go.jp/mscweb/en/himawari89/space_segment/fig/Himawari-8_HRIT_table.xlsx (accessed on 8 September 2022).
67. numpy.linalg.lstsq. NumPy documentation. Available online: <https://numpy.org/doc/stable/reference/generated/numpy.linalg.lstsq.html> (accessed on 14 February 2023).
68. User Guide for EUMETSAT GSICS Corrections for inter-calibration of Meteosat-SEVIRI with Metop-IASI. European Organisation for the Exploitation of Meteorological Satellites. 2020. Available online: <https://www.eumetsat.int/media/45742> (accessed on 3 November 2022).
69. Smirnov, S.; Nizametdinov, I.; Timina, T.; Kotov, A.; Sekisova, V.; Kuzmin, D.; Kalacheva, E.; Rashidov, V.; Rybin, A.; Lavrenchuk, A.; et al. High explosivity of the June 21, 2019 eruption of Raikoke volcano (Central Kuril Islands); mineralogical and petrological constraints on the pyroclastic materials. *J. Volcanol. Geotherm. Res.* **2021**, *418*, 107346. [[CrossRef](#)]
70. McKee, K.; Smith, C.M.; Reath, K.; Snee, E.; Maher, S.; Matoza, R.S.; Carn, S.; Mastin, L.; Anderson, K.; Damby, D.; et al. Evaluating the state-of-the-art in remote volcanic eruption characterization Part I: Raikoke volcano, Kuril Islands. *J. Volcanol. Geotherm. Res.* **2021**, *419*, 107354. [[CrossRef](#)]
71. Prata, A.T.; Grainger, R.G.; Taylor, I.A.; Povey, A.C.; Proud, S.R.; Poulsen, C.A. Uncertainty-bounded estimates of ash cloud properties using the ORAC algorithm: Application to the 2019 Raikoke eruption. *Atmos. Meas. Tech.* **2022**, *15*, 5985–6010. [[CrossRef](#)]
72. Muser, L.O. Combining Aerosol Aging and Data Assimilation for Improving Volcanic Aerosol Forecast. Ph.D. Thesis, Karlsruhe Institut für Technologie (KIT), Karlsruhe, Germany, 2022. [[CrossRef](#)]

73. Bruckert, J.; Hoshyaripour, G.A.; Horváth, A.; Muser, L.O.; Prata, F.J.; Hoose, C.; Vogel, B. Online treatment of eruption dynamics improves the volcanic ash and SO₂ dispersion forecast: Case of the 2019 Raikoke eruption. *Atmos. Chem. Phys.* **2022**, *22*, 3535–3552. [[CrossRef](#)]
74. Harvey, N.J.; Dacre, H.F. Spatial evaluation of volcanic ash forecasts using satellite observations. *Atmos. Chem. Phys.* **2016**, *16*, 861–872. [[CrossRef](#)]
75. Pulkkinen, S.; Nerini, D.; Pérez Hortal, A.A.; Velasco-Forero, C.; Seed, A.; Germann, U.; Foresti, L. Pysteps: An open-source Python library for probabilistic precipitation nowcasting (v1.0). *Geosci. Model Dev.* **2019**, *12*, 4185–4219. [[CrossRef](#)]
76. Dacre, H.F.; Harvey, N.J.; Webley, P.W.; Morton, D. How accurate are volcanic ash simulations of the 2010 Eyjafjallajökull eruption? *J. Geophys. Res. Atmos.* **2016**, *121*, 3534–3547. [[CrossRef](#)]
77. Inoue, T. On the Temperature and Effective Emissivity Determination of Semi-Transparent Cirrus Clouds by Bi-Spectral Measurements in the 10 μm Window Region. *J. Meteorol. Soc. Jpn.* **1985**, *63*, 88–99. [[CrossRef](#)]
78. Watkin, S.C. The application of AVHRR data for the detection of volcanic ash in a Volcanic Ash Advisory Centre. *Meteorol. Appl.* **2003**, *10*, 301–311. [[CrossRef](#)]
79. Závody, A.M.; Birks, A.R. Sun Glint Contamination in ATSR-2 Data: Comparison of Observations and Values Calculated from the Measured 1.6-μm Reflectivities. *J. Atmos. Ocean. Technol.* **2004**, *21*, 787–798. [[CrossRef](#)]

Disclaimer/Publisher’s Note: The statements, opinions and data contained in all publications are solely those of the individual author(s) and contributor(s) and not of MDPI and/or the editor(s). MDPI and/or the editor(s) disclaim responsibility for any injury to people or property resulting from any ideas, methods, instructions or products referred to in the content.